Applied Geochemistry 98 (2018) 152–171

Contents lists available at ScienceDirect

Applied Geochemistry

journal homepage: www.elsevier.com/locate/apgeochem

Evolution of the THC conditions in the FEBEX *in situ* test after 18 years of experiment: Smectite crystallochemical modifications after interactions of the bentonite with a C-steel heater at 100 °C

A.M. Fernández[a,*], S. Kaufhold[b], D.M. Sánchez-Ledesma[a], J.J. Rey[a], A. Melón[a], L.M. Robredo[a], S. Fernández[a], M.A. Labajo[a], M.A. Clavero[a]

[a] CIEMAT – Centro de Investigaciones Energéticas, Medioambientales y Tecnológicas, Dpto. Medio Ambiente, Avda. Complutense 40, 28040, Madrid, Spain
[b] BGR – Bundesanstalt für Geowissenschaften und Rohstoffe, Stilleweg 2, D-30655, Hannover, Germany

ARTICLE INFO

Editorial handling by Thomas Gimmi

Keywords:
FEBEX *in situ* test
Ca−Mg-bentonite
Mg-clays
Iron/Mg-bentonite interactions
Mineralogy
CEC
Crystallochemistry
Corrosion
Hydrocarbon oxidation
Redox state

ABSTRACT

Chemical and mineralogical investigations of the FEBEX repository demonstration experiment after 18 years confirmed those reactions which were identified in previous large scale tests: Fe-corrosion, Mg-accumulation, cation exchange, and mineral dissolution/precipitation. These reactions were mostly restricted to the bentonite-heater contact. However, other processes were detected. Fe oxidation of carbon-containing steel was dominated by oxic corrosion and hydrolysis possibly through a similar Fischer-Tropsch synthesis reaction, leading to the monitored generation of H_2, CO_2 and both reduced (alkanes, alkenes) and oxidized non-volatile (carboxylic acids) hydrocarbons, which are in partial equilibrium with CO_2/carbonate under oxidation states highly reduced. Therefore, temperature, water, oxygen (due to no gas-tight conditions), and other oxidizing agents regulated the redox state and activities of all species involved in the bentonite barrier, being sulfates reduced to H_2S and pyrite, Fe-oxides (hematite/goethite) to magnetite and siderite, and Fe(III)-bearing smectite to saponite and chlorite. These mineral phases were detected as main corrosion products. The dissolved Fe^{2+} ions generated by reduction of Fe-oxides diffused away forming surrounding greenish halos in the bentonite. Because air was not excluded, most of the corrosion was oxic but locally reducing conditions were established.

Significant Mg accumulation was observed at the heater contact, which is related with the highest salinity values of the porewater (Na−Mg−Ca−Cl water-type, 0.41 M ionic strength), the presence of saponite (trioctahedral Mg-smectite), brucite and Fe-rich chlorite; and a modification in the dehydroxylation temperature of the dioctahedral smectite clay mineral particles, together with the precipitation of carbonates and an increase in Ca/Mg at interlayer sites, Na being depleted.

The mechanism for the structural clay mineral alteration seems to be Fe(III) structural reduction, rather than the C-steel heater/liner corrosion. Because Fe^{2+} cations are more stable in trans octahedral sites, rearrangements in crystal lattice seem to have formed cis-trans interstratifications favouring the migration of Mg to octahedral sites and the segregation of Mg^{2+} trioctahedral domains. Thus, both a solid-state transformation, producing high-charge/low charge layers similar to vermiculite ones; as well as dissolution-precipitation transformation, with the crystallization of a trioctahedral Mg-smectite (saponite), brucite and chlorite in localized zones of the bentonite barrier, seem to be inferred, depending probably on $f(O_2)$, temperature, the amount of structural Fe(II) and Mg concentration in the pore water.

The observed clay mineral transformations induced changes in some of the physico-chemical properties of the bentonite, decreasing the total cation exchange capacity and BET surface area. However, these modifications were restricted to the bentonite at close contact with the heater. The rest of bentonite from the FEBEX *in situ* test maintained its performance as an engineered barrier.

* Corresponding author.
E-mail address: anamaria.fernandez@ciemat.es (A.M. Fernández).

https://doi.org/10.1016/j.apgeochem.2018.09.008
Received 30 December 2017; Received in revised form 5 September 2018; Accepted 7 September 2018
Available online 22 September 2018

1. Introduction

Bentonites are one of the most important industrial raw materials, widely used for different technological applications. Furthermore, bentonites are an essential component of the multi-barrier system securing the long-term safety of the final disposal of nuclear wastes. The efficiency of such engineered clay barrier relies on its physical and chemical confinement properties: low permeability, low diffusivity, high retention and swelling capacity.

An important issue for performance assessment is to demonstrate the long-term preservation of the bentonite properties, i.e., hundreds of thousands of years under real conditions of a repository. The challenging scientific approach used to tackle the problem of predicting long-term clay barrier behaviour is analysing the results from experiments conducted in underground research laboratories (URL) at real scale and at real conditions (Tournassat et al., 2015). Around 40 years ago few commercial high quality bentonites were acquired to study bentonites as buffer and backfill materials in the construction of engineered barrier systems (EBS) for the isolation of high-level radioactive waste (e.g., MX-80, Calcigel, etc.). The selected natural bentonites were industrially processed to fabricate highly compacted bentonite blocks, which have been used in different *in situ* large-scale EBS experiments (e.g., FEBEX *in situ*, LOT, Prototype, TBT, etc.) and Mock-Up tests (FEBEX, OPHELIE, China-Mock-Up, etc.). The aim was to analyse the properties, manufacturing, handling and long-term performance of the buffer (e.g., Kaufhold and Dohrmann, 2016; Dohrmann et al., 2013 and references therein).

In different laboratory and large-scale tests some specific processes in the bentonite were observed as consequence of interactions with groundwater inflow, heat gradients and steel contact from heaters simulating canisters. The main processes occurred in the whole bentonite mass were cation exchange and dissolution/precipitation reactions (e.g., Karnland et al., 2009; Fernández and Villar, 2010; Olsson et al., 2013; Kaufhold et al., 2013, 2015; 2017; Kumpulainen et al., 2016). Other types of processes were observed at the bentonite-heater contact: metal corrosion, Mg accumulation and smectite alteration towards trioctahedral 2:1 magnesian clay minerals (e.g., saponite); illite and/or illite/smectite mixed-layers (I/S MLs) being absent (Fernández and Villar, 2010; Kaufhold et al., 2013; Svensson et al., 2011; Svensson, 2015).

In terms of chemical behaviour, carbon steel is unstable in presence of water and canisters are expected to corrode at the long-term stable anoxic/anaerobic repository conditions. Iron-oxyhydroxides as corrosion products are produced during the aerobic phase of the repository due to different iron-clay interactions, in which all the oxygen available in the system is consumed. When corrosion of metallic iron or steel occurs in reduced conditions, aqueous iron (Fe^{2+}) is released in solution and hydrogen is produced as result of the dissociation of water and the reduction of protons, leading to a pH increase and a decrease in the redox potential. At these conditions, magnetite is produced as corrosion product, as well as siderite, sulfides and iron silicates (Fe-serpentine-type minerals, greenalite, cronstedtite). The actual mineral paragenesis of corrosion products results from the competition between the mineral dissolution and precipitation kinetics, the local geochemical conditions (pH and Eh) and the transport of reaction products (Tournassat et al., 2015). Furthermore, variables such as time, temperature, water:clay ratio, iron:clay mass, crystal chemistry of the initial clay-rich materials, and pore fluid compositions are critical driving forces for the type and amounts of solid products neoformed (Mosser-Ruck et al., 2010).

Much of the structural iron in clay minerals is ferric iron, which can be reduced either chemically or biologically, structural Fe(III) acting as an electron acceptor. It is known that the reduction of structural Fe(III) causes small and fully reversible and non-reversible changes in the structure and chemistry of a clay mineral and/or its reductive dissolution (e.g., Stucki, 2011; Gorski et al., 2013). This depends on many factors, including the nature of the clay mineral (i.e. iron content, layer charge, and crystal chemistry), the extent of reduction (< 30%: stable), the chemistry of the aqueous medium and the presence of microorganisms (Dong, 2012).

On the other hand, increases of magnesium are of interest for the performance of the bentonite barrier (e.g., Kaufhold et al., 2016), because they may point to structural transformations and compositional changes which affect the stability of the smectite over time inducing the formation of crystallized 2:1 magnesium phyllosilicate minerals, such as the trioctahedral saponite as end-member, 2:1:1 magnesium phyllosilicate minerals (Chl/S ML and chlorites) or brucite-like sheets ((Al, Mg)—OH phases). Therefore, bentonite interactions at heater interface, where the corrosion of iron (C-containing steels) and iron- and Mg-rich porewater-bentonite interactions occur, are an important issue for safety assessment calculations, because it might result in the transformation of smectite, main active component of the bentonite buffer, to non-swelling silicates, which would affect the bentonite barrier performance.

The FEBEX *in situ* experiment is a demonstration and research project that was performed in a gallery excavated in granite in the Grimsel Underground Research Laboratory (URL) at Switzerland. It is based on the former Spanish reference concept in crystalline rock in which the canisters are placed horizontally in drifts and surrounded by a clay barrier constructed of highly compacted bentonite blocks (Fig. 1). A horizontal drift with a diameter of 2.28 m was excavated in the Grimsel granodiorite in 1995 (Huertas et al., 2006). Two electrical heaters, of the same size and of a similar weight as the reference canisters, were placed in the axis of the drift. The gap between the heaters

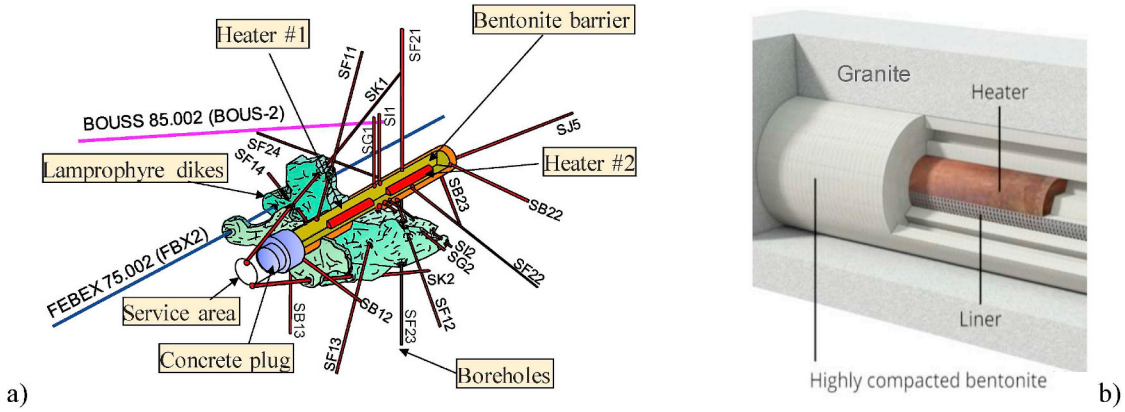

Fig. 1. a) Scheme of the FEBEX *in situ* test during the First Operational Phase (1996–2002) when the two heaters where running (Farias, per. comm.), b) Detail of the bentonite blocks surrounding the liner and the heater (Nagra).

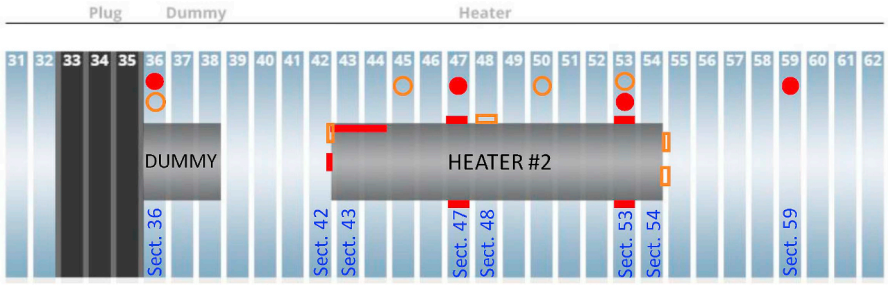

Fig. 2. Schematic figure of the FEBEX *in situ* test divided in dismantling sections: location of the dismantling bentonite sections around Heater #2 selected for THC studies (in orange: samples analysed by BGR; in red: samples analysed by CIEMAT). (For interpretation of the references to color in this figure legend, the reader is referred to the Web version of this article.)

and the rock was backfilled with compacted bentonite blocks, up to a length of 17.40 m. The construction of the concrete plug, which sealed the backfilled area, was completed in October 1996, and the heating operation started on 27th February 1997. A constant temperature of 100 °C was maintained at the heaters/bentonite interface, while the bentonite buffer was slowly hydrating with the water naturally issuing from the granitic rock formation. The total water inflow for the entire test zone varied from 4.5 to 8.5 mL/min, the most frequent hydraulic conductivity being $1{\cdot}10^{-11}$ m/s; and the hydraulic pressure along a horizontal plane through the axis of the gallery at a distance of 50 m being ~0.72 MPa. Two main operational phases were executed: a) the First Operational Phase (1996–2002), which corresponds to the FEBEX-I and FEBEX-II projects, finishing with the dismantling of the Heater #1, and b) the Second Operational Phase (2002–2015), which finished with the dismantling of the Heater #2 within the FEBEX-DP Project.

The dismantling of the second part of the FEBEX *in situ* test provided the opportunity to quantify the modifications of the bentonite after reacting due to changes in the initial physico-chemical conditions and, among others, the perturbations linked to the interactions between the bentonite and the allochthonous engineered solid materials, such as the carbon steel from the heaters, acting as an analogous component of the canisters confining the nuclear waste. The FEBEX *in situ* experiment allows to analyse the iron- and Mg-rich porewater-bentonite interactions at real conditions of a HLW repository system because: a) it is a real scale experiment, with similar boundary conditions occurring in the near field, b) it is the longest real scale *in situ* experiment up to date, and c) it has performed during the longest period of time (18 years of heating and hydration).

The aims of this paper are: a) to describe the final mineralogical and geochemical state of FEBEX bentonite samples at very close contact with the liner/Heater#2 after 18 years of experiment, b) to identify possible structural alterations of the smectite clay mineral by effect of heat and iron- and Mg-rich porewaters-bentonite interactions, and c) to identify changes in the physico-chemical properties of the bentonite induced by mineral transformations.

2. Materials

2.1. The bentonite

The bentonite barrier utilized in the FEBEX *in situ* test was fabricated by using a Ca−Mg-bentonite material, named FEBEX bentonite (Supplementary Table S1). A complete characterization of the material can be seen in Huertas et al. (2006) and Fernandez et al. (2004). This bentonite came from the Cortijo de Archidona deposit, developed by Minas de Gádor, S.A., in the zone of Serrata de Níjar (Almería, Spain). About 300 tons of raw material, homogenized and conditioned, were acquired for the fabrication of the blocks for the barriers of the two large-scale tests and for all laboratory tests. Some properties that characterize this bentonite are the following (Fuentes-Cantillana et al., 2000; Huertas et al., 2006): a) montmorillonite content: 88–96 wt.%; b) specific weight: 2.67–2.75 kg/dm^3, c) swelling pressure for a dry density of 1.60 g/cm^3: 4–6 MPa, and d) saturated hydraulic conductivity for a dry density of 1.60 g/cm^3: $4.2{\cdot}10^{-14}$-$7.6{\cdot}10^{-14}$ m/s.

The raw material prepared for the fabrication of the blocks was a granulate of bentonite with less than 5% of the grains greater than 5 mm, with more than 85% of the grains less than 74 µm. The clay barrier was formed by blocks, weighing 20–25 kg each, of highly-compacted bentonite. The weighted average values of the dry density and water content of all the blocks were 1.70 g/cm^3 and 14.4%, respectively. The construction of the barrier used 5331 blocks, which corresponds to a mass of 115.7 ton. The in-place barrier had an average dry density of 1.60 g/cm^3 and a volume, when installed, of construction gaps (separations of variable magnitude) of 5.53%.

2.2. Sampling during the dismantling of the heater #2

The second dismantling operation of the FEBEX *in situ test* (Heater #2) began on 17th February 2015 and 8th May 2015 with the drilling of cores in the concrete plug and the bentonite dismantling and sampling, respectively; and finished on 5th August 2015. During this period, different bentonite samples were obtained for performing different studies. Heater #2 was switched off on 24 April 2015, 14 days before starting the bentonite dismantling operations.

For thermo-hydro-chemical (THC) and thermo-hydro-mechanical (THM) studies an exhaustive post-mortem bentonite sampling and analysis program was performed (Garcia Siñeriz et al., 2016; Villar et al., 2017). Bentonite blocks were sampled at different sections along three radii, as well as other bentonite samples at contact with the liner/Heater #2 (Fig. 2). For the iron- Mg-rich porewater-bentonite interaction studies, specific bentonite and protrusion samples were analysed in this study:

- Bentonite blocks, core samples or samples located at the frontal (Section 42) and rear (Section 54) side of the Heater #2: BMS-42-xx, BMS-48-xx and BMS-54-xx samples, being x = 1, 2, ... the number of the collected sample (Supplementary Fig S1, Fig. S3, Fig. S5 and Fig. S10).
- Bentonite blocks located around Heater #2: Section 47 and 53 (Supplementary Fig S2, Fig S4).
- Bentonite samples located at the liner contact (external part of the liner) at Section 47 and Section 53: BMS-47-xx and BMS-53-xx samples (Supplementary Fig S2, Fig S4, Fig. S6)
- Bentonite protrusions found inside the liner holes (internal part of the liner) around the Section 42 and Section 43 (Supplementary Fig. S7 and Fig. S9), and bentonite from the frontal part of the Heater #2 (Supplementary Fig. S8). Both types of samples were the closest bentonite samples to the contact of the Heater #2.

The samples were obtained *on site* mainly with the use of an electric percussion hammer with a flat-end bit tool attached or by using a standard drilling machine provided with the desired inner diameter barrel (70–100 mm in diameter and 10–280 cm in length). Most of the samples were wrapped in plastic film inside the FEBEX gallery after their extraction and then transported out of the gallery where a final preservation inside double vacuum-sealed aluminium-foil bags was

performed. A second durable plastic bag and protection against mechanical actions was used to ensure the integrity of the material. Therefore, the samples were retrieved and collected with minimal exposure to the atmosphere (few hours) before packing.

Protrusion samples were jointly taken *on site* by BGR and CIEMAT, which were preserved in plastic bags. CIEMAT samples were preserved in turn in Al-foil bags.

2.3. Bentonite-metal (BM) and protrusion samples: subsampling at laboratory

The samples received from the Grimsel Test Site were stored in a humidity chamber at 15 °C and then at laboratory conditions at a temperature between 18 and 22 °C, except for the samples which were stored in a refrigerator. The samples were sliced with a knife in several parts as a function of the Heater#2 contact (see Fernández et al., 2018; Kaufhold et al., submitted and Supplementary Fig. S11 to S13 for further information). BGR analysed samples from Sections S42, S54, S48 and S54, whereas CIEMAT analysed samples from Sections S47 and S53 (Supplementary Fig. S6). BMS and protrusion samples were subsampled with a knife or a magnet for different analyses (Supplementary Fig. S14).

3. Methodology

3.1. Physical properties

The gravimetric water content, *w.c.,* is defined as the ratio between the weight of water and the weight of dry solid expressed as a percentage. The weight of water was determined as the difference between the weight of the sample and its weight after oven drying at 110 °C for 48 h (weight of solid).

Dry density, ρ_d, is defined as the ratio between the weight of the dry sample and the volume occupied by it prior to drying. The volume of the specimens was determined by immersing them in a recipient containing mercury and by weighing the mercury displaced, as established in UNE Standard 7045 “Determination of soil porosity”.

3.2. Mineralogical analysis: XRD, FTIR, thermal analysis, SEM and TEM

XRD diffraction patterns were obtained from random powders and oriented aggregates. The bulk sample powders were obtained by grinding the samples in a RETSCH RM 100 mortar grinder with a pestle of agate to a size of less than 63 μm after drying them at ambient temperature. The powders were analysed with a Philips X'Pert –PRO MPD diffractometer, using an anticathode Cu-K_α at 45 kV and 40 mA, equipped with a fixed divergence slit (0.1245° size), Scientific X'celerator detector. The samples were investigated from 2° to 70° 2θ with a step size of 0.017° 2θ, and a scan rate of 50 s per step for the powder samples. The XRD database used for mineral identification has been the Power Diffraction File from the International Center for Diffraction Data (ICDD).

The modified Jackson (2005) treatment was used to separate the clay minerals from the rock matrix (Moore and Reynolds, 1989). The fine fraction of less than 2 μm was obtained by suspension and sedimentation in deionised water. The final clay suspension was ultrasonic dispersed using 1 g in 5 mL of deionized water. Oriented mounts were prepared by suction of the dispersion through 3 mm thick ceramic tiles by applying vacuum. These clay films (air dried, ethylene glycol solvated and 550 °C heated) were X-rayed from 2 to 35° 2θ using a Bruker D8 Advance diffractometer with an anticathode Cu-Kα at 40 kV and 30 mA, equipped with a fixed divergence slit (0.15° size). The samples were investigated a step size of 0.02° 2θ, and a scan rate of 2 s per step.

Fourier Transform Infrared (FTIR) spectroscopy is complementary to X-ray diffraction and other methods. Fourier transform IR spectra were obtained at CIEMAT in the middle-IR region (4000-400 cm^{-1}) with a Nicolet 6700 with a DTGS KBr detector (resolution 4 cm^{-1}, 32 scans) on KBr-pressed discs in transmission technique in an atmosphere continuously purged from water and atmospheric CO_2. Two milligrams of powdered air-dried sample were dispersed in 200 mg of KBr and pressed to a clear disc. The pressed samples were analysed at room temperature and then after heating in an oven overnight at 110 °C.

Thermal Analysis (TG/DSC) of the bulk sample was performed at CIEMAT in a Setaram Setsys Evolution 16 equipment at a heating rate of 10 °C/min and under a dynamic argon atmosphere (20 mL/min) at temperatures between 20 °C and 1100 °C.

Scanning electron microscopy (SEM). A ZEISS EVO LS 15 SEM microscope coupled to a X LINK LZ_5 energy dispersive X-ray energy spectrometer (XEDS), which allows for the qualitative analysis of light elements from boron, were used to define the microstructural morphology of clay minerals, possible alteration products and accessory minerals at CIEMAT. Most of the clay samples were dried at 40–60 °C in an oven overnight, and then subjected to a gold metallization by applying $5{\cdot}10^{-2}$ Torr vacuum and a gold coating of 300–400 Å thickness, using a BALZERS SCD 004 sputter coater for the scanning electron microscopy analysis.

Transmission Electron Microscopy (HRTEM). JEOL JEM 3000F microscope working at 300 kV accelerating voltage, 0.17 nm of resolution, and coupled to an OXFORD INCA energy dispersive X-ray energy spectrometer (XEDS), which allows for the qualitative analysis. Clay particles (< 2 μm fraction) were fully dispersed in isobutanol by shaking and ultrasonic treatment. A tiny drop of the clay suspension was pipetted and deposited on holey carbon formvar coated copper TEM grids.

TEM analysis was performed mainly for determining the structural formula of the clay minerals, and to observe the thickness of the structural units perpendicular to the plates (c-axis and/or a- or b-axis). The EDS analyses were obtained from more than five determinations per sample. Based on them, structural formula of the clay particles was calculated as average (Moore and Reynolds, 1989). The procedure is based on a formula unit with 11 oxygens (4 cations from tetrahedral sheet and 2 from the a dioctahedral octahedral sheet) for dioctahedral smectites and illites; 14 for chlorites [$\ldots O_{10}(OH)_2{-}1H_2O$]; and 7 for kaolinites [$\ldots O_5(OH)_4{-}1H_2O$]. Cations are assigned to the tetrahedral sheets first. If there are less than 4 Si cations per formula unit Al is taken to fill the tetrahedral sites. The remainder of the Al cations are assigned to the octahedral sheets together with Fe, Mg, Mn and Ti. Ca, Na and K are assigned to the interlayer sites. Mg is assigned to interlayer sites depending on the sum of octahedral cations: 2 for dioctahedral clays and 3 for trioctahedral clay minerals; and the total layer charge of the structure: between 0.2 and 0.6 for smectites; 0.6 to 0.9 for vermiculites; and 0.6 to 1 (or 2) for illites (or brittle micas). EDS does not differentiate between the oxidation states of iron, so all iron was considered as Fe^{3+}, except for chlorites where all Fe was considered as Fe^{2+}. For comparison, each structural formula was obtained both according to Moore and Reynolds (1989), i.e., with all magnesium at octahedral sites; or by fixing the sum of octahedral ions to 2.0; i.e., allowing some amount of magnesium at interlayer sites. However, the latter option was considered for crystal chemistry studies. If all magnesium is taken at octahedral sites, the limit of 2.09 per $O_{10}(OH)_2$ indicates a departure from the dioctahedral mineral structure. The layer charge of 0.66 (smectite of high charge, HC) per $O_{10}(OH)_2$ is the upper limit of expandable phases (de la Calle and Suquet, 1988).

3.3. Geochemical analysis of the bentonite

3.3.1. Chemical composition by X-Ray fluorescence

The major elements (SiO_2, Al_2O_3, Fe_2O_3, MnO, MgO, CaO, Na_2O, K_2O, TiO_2, P_2O_5 and SO_3 in wt.%) were analysed by X-Ray Fluorescence Analysis (XRF) in natural powdered samples, which were ground to < 250 μm. The XRF analyses were performed on an Axios spectrometer from Panalytical equipped with a rhodium X-ray tube

(stimulation power: 1 KW). The dissolution or decomposition of the sample into a homogeneous glass was obtained by fusion, which consisted on heating a mixture of sample and flux ($Li_2B_4O_7$) at high temperatures (800–1000 °C) so that the flux melts and the sample dissolves. The end product after cooling is a one-phase glass.

Powdered samples (0.8 g of oven-dried samples at 105 °C) were homogeneously mixed with 7.2 g of lithium tetraborate in the proportion of 34–66%. The whole material was molten stepwise in a platinum crucible at a smelting apparatus. After this procedure, the melt was transferred into a platinum jacket and cooled. The loss of ignition was determined separately by oven-drying the dried sample at 1025 °C for 3 h.

3.3.2. Total carbon, total inorganic carbon and total sulfur

Total Carbon, total sulfur and total inorganic carbon were determined on 0.2 g of powdered solid samples obtained from a representative and homogeneous sample. The powders were obtained by grinding the air-dried samples in a RETSCH RM 100 mortar grinder with a pestle of agate to a size of less than 250 µm. Total Carbon (TC) and Total Sulfur content were determined on the solid sample by means of a LECO CS-244 analyzer by combustion. The total inorganic carbon (TIC) content was obtained with a TOC-V_{CSH} analyzer (SHIMADZU, Shimadzu Scientific Instruments, Kyoto, Japan) equipped with a SSM-5000A module. The presence of organic carbon was evaluated by the difference between TC and TIC.

3.3.3. Fe(II)-Fe_{total} in the samples at contact with the liner and heater

Fe(III) and Fe(II) were leached from the samples by using a modification of the procedure described in Tarafder and Thakur (2012) and analysed by 1,10 phenantroline spectrophotometric method.

To a finely ground sample of 0.1–0.2 g, 1 g of NH_4HF_2 and 10 mL of 1:1 H_2SO_4 were added to a 40 mL high-density polyethylene (HDPE) tubes. The tubes were closed with caps and heated to 90 °C for 60 min in a shaking water bath. After this extraction process, the tubes were allowed to cool to room temperature. The contents were transferred to 50–100 mL volumetric flasks and made up to volume with MilliQ water.

For the spectrophotometric determination of Fe(II), a 1–5 mL aliquot (duplicate) was taken in a 50 mL volumetric flask; 5 mL of 6 M sodium acetate and 1 mL of 1% 1.10 phenanthroline were added, mixed well and made up to volume with MilliQ water. After 15 min, the absorbance at 510 nm was measured against a blank of reagents.

For the spectrophotometric determination of total-Fe, another aliquot (duplicate) was taken in a separate 50 mL volumetric flask and 2 mL of 10% hydroxylammonium chloride were added to it. This was mixed well and was allowed to stand 20 min. Then, 5 mL of 6 M sodium acetate and 1 mL of 1% 1.10 phenanthroline were added, mixed well and made up to volume with MilliQ water. After 15 min, the absorbance at 510 nm was measured against a blank of reagents.

The contents of iron were determined in the samples from the calibration curve prepared from iron standard solutions. The estimation of ferric iron was made by subtracting the ferrous iron content from the total iron content.

3.4. Physico-chemical characterization

3.4.1. Cation exchange capacity

Total CEC was measured with 0.01 M copper triethylenetetramine, Cu-Trien or $[Cu(trien)]^{2+}$, solution (Ammann et al., 2005). 200 mg of clayey sample were weighed in 60 mL centrifuge tubes. 25 mL of deionized water were added, and the suspension was dispersed by ultrasonic treatment for 5 min. Then, 10 mL of 0.01 M $[Cu(trien)]^{2+}$ were added and allowed to react by end-over-end shaking for 1 h. After this procedure, a complete exchange of the $[Cu(trien)]^{2+}$ complex with the exchangeable cations is guaranteed. Afterwards, the suspensions were centrifuged at a constant rotation speed of 15500 rpm for 20 min. 3 mL of the clear blue solution (filtered through 0.45 µm pore size syringe filter) were filled into 1 cm optical glass cuvettes and the absorbance of the solution was measured at 578 nm wavelength by using a Merck spectrophotometer. The analyses were performed on duplicate. The standard deviation of the measurement is ± 2 meq/100g.

3.4.2. Cation exchange population

The determination of the cation exchange population was performed by using Cs as index cation (Sawhney, 1970). Caesium acts as a highly selective cation to displace all exchangeable cations from the clay minerals if its concentration is sufficiently high. Solid samples were equilibrated inside a JACOMEX glove box (< 1 ppm O_2) at 1:4 solid to liquid ratio (0.25 kg/L) with 0.5 M $CsNO_3$ at pH 8.2. After phase separation by centrifugation (outside the glove box), the supernatant solutions were filtered through 0.45 µm pore size syringe filter (inside the anoxic glove box), and the concentration of the major cations was analysed.

3.4.3. BET and external surface area

Classical nitrogen adsorption/desorption isotherms were obtained on a discontinuous volumetric sorptometer, Micromeritics ASAP 2020 V3.02 H. Approximately 0.5 g of total sample were ground in an agate mortar. The samples were dried at 90 °C during at least 24 h before the tests. Prior to the nitrogen adsorption, the samples were out-gassed by heating at 90 °C for 18 h using a mixture of helium and nitrogen under a residual vacuum between 500 and 6–10 µmmHg. The tests were performed at the boiling point of liquid nitrogen (77 K) considering a molecular cross section area of 0.162 nm^2 for the nitrogen molecule. External surface areas were calculated using the standard N_2-BET method, using a series of data points over the P/P_0 range of 0.02–0.25 on the nitrogen adsorption isotherm (Gregg and Sing, 1982).

3.4.4. Soluble salts by aqueous leaching

The soluble salts have been analysed in aqueous extract solutions. The subsamples were crushed without previous drying, and placed in contact with deionised and degassed water at 1:4 solid to liquid ratio, shaken end-over-end and allowed to react for one day under anoxic conditions inside an anoxic glove box with oxygen content below 1 ppm. After phase separation by centrifugation (30 min at 15500 rpm), the supernatant solutions were filtered through a 0.45 µm pore-size syringe filter (inside the anoxic glove box) and analysed.

3.5. Water chemical analyses

The water samples were filtered through 0.45 µm syringe filters, except those for pH and electrical conductivity (EC) measurements. The pH was measured by means of an ORION 720A pH-meter equipped with a Metrohm 6.0224.100 combined pH micro-electrode. Merck pH buffer solutions of pH 4.0 and 7.0 were used for pH-meter calibration.

The total *alkalinity* of the water samples was determined with a specific Dynamic Equivalence Point Titration (DET) method for analysing samples of 1–2 mL. The instrumentation consists of a Metrohm 888 Titrando equipment with a 5-mL burette and a 6.0224.100 Metrohm combined pH micro-electrode. The *major and trace cations, including silica,* were analysed by Inductively Coupled Plasma Optical Emission Spectrometry (ICP-OES) in a Varian 735ES spectrometer. Sodium and potassium were determined by atomic absorption spectrometry in an Agilent AA 240 FS spectrometer. A*nions* were analysed by ion chromatography (Dionex ICS-2000).

The methodology behind BGR derived results were reported elsewhere (Kaufhold et al., subm.).

Table 1
Neoformed mineral phases observed in the samples at direct contact with the liner/Heater#2 by means of XRD, FTIR and TG-DSC techniques.

Type of mineral phases	Mineral phases	Samples
Fe-oxyhydroxides	Goethite (weak FM)	BMS-42-2 (1 mm, 1 cm), E2, E5, E6, BMS-47-3 black, BBIL-42 magnet, S43 black magnet, RNW42 magnet
	Magnetite (FM)	E6, BMS-42, BMS-47-2 black purple, BMS-47-2 magnet, BMS-47-3 black, RV-42 green magnet, BSH, BBIL-42 magnet, S43 black, WB-42 magnet, RNW42 magnet
	Titanomagnetite	S43 black
	Maghemite (FM)	E6
	Hematite (AFM)	E6, BMS-47-2 magnet, WB-42, S43 black, GB-42, BMS-47-1[(2)], BMS-53-1[(2)]
	Ferrihydrite	BMS-42-2[(3)]
Carbonates	Aragonite	E7, WP, BSH, RV-42 green magnet
	Dolomite	E7, BMS-47-2 black-purple, BSH, CL
	Magnesite	BSH
	Siderite	E6, BBIL-42 magnet, S43 black magnet
Sulfides	Pyrrhotite	BMS-47-2 green, RV-42 green magnet, S43 black
	Mackinawite	BMS-47-2 black-purple, WB-42
	FeS	S43 black magnet, WB-42
Mg-hydroxides	Brucite	BMS-54-5B [(1,2,3)], S43 black, RV-42 green, BSH, GB[(2)]
Chlorites	Clinochlore/Chamosite	BMS-47-2 green, BMS-47-2 magnet, GB-42, CL, BB[(1,2)], BPB
Mg-smectite	Saponite	BMS-42, GB-42, S43 black, BMS-47-2 magnet, BMS-47-1, 2,3[(3)], BMS-53-1,2,3[(3)], CL, CL[(3)], RV-42 green[(3)], RNW42[(3)], GB-42, GB-42[(3)]

XRD: non-numbered samples and denoted with [(1)]; [(2)]FTIR; [(3)]TG-DSC. FM: ferromagnetic, AFM: antiferromagnetic.

4. Results

4.1. Mineralogical analysis

4.1.1. X-ray diffraction

Apart from the main minerals of the reference sample (Ca−Mg smectite, quartz, cristobalite, feldspars and calcite), neoformed minerals were found both in the BMS (above the liner) and protrusion (inside liner holes) samples (Table 1). Aragonite was found in the white powder adhered to the internal part of the liner (WP), at direct contact with the Heater #2 (Supplementary Fig. S7a), as well as in protrusion samples. Apart from calcite; dolomite, siderite and magnesite were also detected by XRD. Iron corrosion products found were: a) ferromagnetic minerals: magnetite, titanomagnetite and hematite (ferrihydrite was only detected by TG-DSC); and b) weak ferromagnetic minerals: goethite (Fig. 3a). S-phases were also detected as FeS, mackinawite, and pyrrhotite. Other mineral phases were celestine, anatase and rutile. Brucite was detected in the protrusion samples with a black-greenish color (RV-42 and BSH) (Fig. 3b).

With respect to the clay minerals, Ca−Mg-montmorillonite was the main clay mineral phase (> 85-90 wt.%), but changes in the d(060) reflexion were observed in some samples indicating a modification of the clay mineral structure. Apart from the d(060) reflexion at 1.49 Å of dioctahedral smectites, a peak at 1.53–1.52 Å (Fig. 3d) appears in some samples (RV-42 green), indicating the presence of clay minerals of trioctahedral character. Saponite seems to appear in some samples analysed by CIEMAT (BMS-47-2; GB-42 green-black and CL green bentonite), and in the E5 and E6 samples (Kaufhold et al., subm.).

The presence of trioctahedral smectites was also analysed in the BMS-54 samples (see Kaufhold et al., subm.). Sample BMS-54-5B1, with

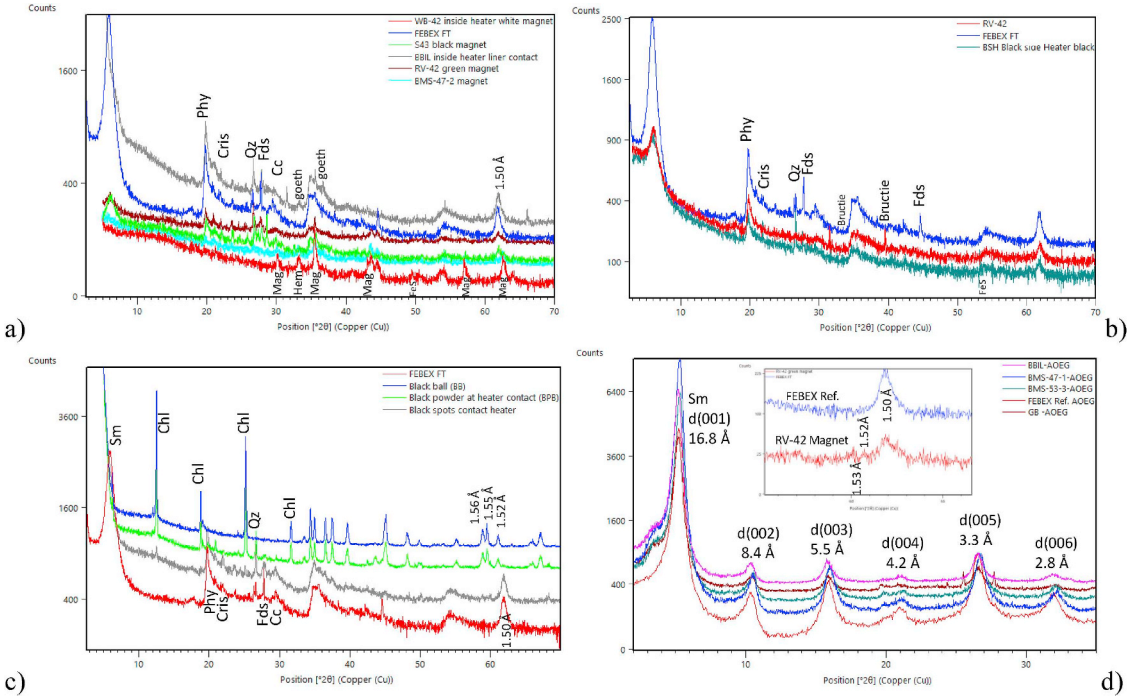

Fig. 3. XRD patterns of bulk samples from BMS and protrusion samples located at contact with the liner/Heater #2: a) Fe-oxy-hydroxides from magnetic samples; b) brucite; c) chlorite at the frontal part of the Heater #2, and d) ethylene-glycol solvated oriented aggregates.
Phy: phyllosilicates; Crs: cristobalite; Qz: quartz, Fds: feldspars; Cc: calcite, goeth: goethite; Mag: magnetite; Hem: hematite; Sm: smectite; Chl: chlorite.

the largest MgO increase (see below), shows a new peak at 1.54 Å, which indicates the presence of trioctahedral domains or phases. XRD Rietveld refinement of the patterns from BMS-54 samples at very close contact with the liner/Heater#2 revealed also the presence of brucite. Kaolinite and other types of clay minerals were ruled out based on oriented mounts XRD. Because brucite does not explain the change of the (060) reflection, the formation of both, brucite and trioctahedral smectite are involved. However, XRD Rietveld refinement did not reveal a decrease of the smectite content although the CEC was markedly reduced as shown below.

On the other hand, chlorite seems to appear in some samples analysed by CIEMAT (BMS-47-2; GB-42 green-black and CL green bentonite), but especially in the samples taken at the frontal part of the Heater #2: the black scraping powder obtained from a block (Supplementary Fig. S8, BPB) and a separated piece (Supplementary Fig. S8, BB) (Fig. 3c). As shown below, chlorite was also detected by SEM and FTIR techniques.

However, when analysing the < 2 μm fraction, a fully expansible Ca−Mg-montmorillonite was the main phase (Fig. 3d), corresponding to a R0 S/I mixed layer. In the retrieved samples the calculated percentage of illite layers between the smectitic phase is ~10 ± 1%, which is similar to that found in the reference bentonite (8% of illite layers in the R0 I/S ML, Fernández et al., 2018). No other mineral phases, such as illite, I/S ML or chlorite were identified in the oriented aggregates performed with the < 2 μm fraction.

4.1.2. FTIR analysis

In general, the spectra from the bulk samples contain the main typical dioctahedral smectite bands, as well as quartz (Fig. 4).

Hematite and goethite were also observed by FTIR in the BMS (BMS-47-1, BMS-53-1) samples at direct contact with the liner (Table 1). Aragonite, calcite and quartz were the main minerals from the white powder (WP) adhered to the liner surface (Fig. 4). In most of the samples analysed, no changes were found, except in the GB and RV-42 green samples where possible modifications in the smectite clay mineral structure were found; and in the black ball (BB) sample (Fig. 4), where chlorite was identified. An increment of the δMgFeOH stretching band at 3563 cm^{-1} as well as a decrease of the δAlAlOH bending band at 914 cm^{-1} were detected in the black (BSH), black-reddish (BBIL) and reddish (S43-FR) material, slightly increasing the δAlFeOH band at 885 cm^{-1} in the BBIL and BSH samples. An increase in the δAlMgOH bending band at 840 cm^{-1} was also observed in the RV-42 black-greenish sample.

In the black-greenish (GB) material new bands at 3700 and 705 cm^{-1} were distinguished, indicating the presence of Mg_3OH vibrations, such as in trioctahedral structures. Farmer (1974) attributed this band close to 3700 cm^{-1} to Mg_3OH vibrations in dehydrated saponites containing interlayer Na or K, whereas Van del Marel and Beutelspacher (1976) and Bergaya et al. (1985) to chlorite/smectite mixed-layers; Pelayo et al. (2018) to smectite with intermediate composition between beidellite and Fe-rich saponite; and Madejová (2003) to outer AlAlOH vibrations in kaolinite. Kaolinite can be excluded since it has not been identified by XRD. This new band at 3698 cm^{-1} was also observed in the BMS-54-5B1 studied by BGR, with a high MgO content (Kaufhold et al., submitted). In this sample, slight changes were also observed in the oxide deformation range (400–600 cm^{-1}) of the spectrum, where both additional humps (570 + 440 cm^{-1}) can be explained by a larger brucite content, because the pure brucite also reveals bands at these positions and kaolinite was not observed in the XRD analyses. Brucite and saponite were identified by XRD and TG-DSC analyses (see below) in the BMS and protrusion samples (Table 1).

In the case of the BB sample, a Fe-rich chlorite containing aluminium was detected (Fig. 4). This chlorite shows bands at 3547 and 3409 cm^{-1}, which are associated with the OH-stretching vibrations of the interlayer hydroxide sheet. The exact position of this doublet (at 3565 and 3434 cm^{-1} theoretically) varies with composition, shifting to lower frequency with increasing Al and Fe content. The band at 3547 cm^{-1} indicates high substitution of Mg by Fe at octahedral sheets (MgFeOH vibration). The band at 3650 cm^{-1} is related with OH-stretching vibrations of the inner hydroxyl groups at octahedral sheets, close to the unsubstituted brucite position (Mg_3OH ~ 3698 cm^{-1}). The shift of the stretching Mg_3OH vibrations towards lower frequencies (~3650 cm^{-1}), as well as the non-marked splitting of the principal Si−O band at 998 cm^{-1}, reflect some Al-for-Si substitution in the tetrahedral sheet in the 2:1 layer. The band around 667 cm^{-1} comprise OH deformation components from the 2:1 layer and the theoretical Mg-hydroxide sheet. This band is strongly dependent on the composition of the interlayer octahedral sheet and is splitted into two components (664 and 637 cm^{-1}) when Fe content increases (Russell, 1987). The bending vibrations of Mg−O−H groups are observed at 664 cm^{-1}, but those for the Al−O−H groups are also observed at 750 cm^{-1}. With increasing substitution of Mg by Al, chlorites become more dioctahedral, and on contrary increasing Mg, chlorites become more trioctahedral. However, the 3547 and 3409 cm^{-1} doublet suggest that the hydroxide sheets have also a trioctahedral character.

4.1.3. TG-DSC analysis

Significant differences were found in the TG-DSC curves of the analysed retrieved samples, which indicate the presence of corrosion by-products and a structural modification of the smectite clay mineral in the samples at close contact with the Heater#2 (Fig. 5). These changes were observed both in the BMS material, taken from direct contact with the liner, and in the protrusions samples, taken from inside the liner holes. Ferrihydrite was identified in the magnetic material of the BMS-47-2 sample. Other Fe-oxyhydroxides were detected in the BBIL-42 and RV-42 green samples (Table 1). The BGR analysis of the curves of the H_2O and CO_2 evolved gas from Ex-protrusion samples confirmed the presence of goethite (dehydroxylation at 300 °C), which was also found by XRD (in E2, E5, E6 samples); and carbonates (siderite and aragonite by XRD in E6 and E7 samples).

When the DSC curves are compared (Fig. 5), GB and RV-42 green protrusion samples show a new peak around 492 °C. This peak is assigned to brucite, $Mg(OH)_3$, corroborating the $Mg(OH)_3$ vibrations observed by FTIR analyses. This was also confirmed in the BMS-54 samples analysed by BGR, where a new peak appeared at about 530 °C in the water curve, which was assigned to brucite.

Furthermore, apart from the main dehydroxylation peak at around 650 °C (typical of dioctahedral smectites), two new peaks between 520 and 550 °C and between 592 and 622 °C appear in the total fraction (Fig. 5), which are only observed between 520 and 550 °C in the < 2 μm fraction (Fig. 6). These peaks are observed both in the BMS and in the protrusion samples. The presence of these additional and/or abnormal dehydroxylation peaks indicates the presence of another type of clay mineral in addition to the cis-vacant dioctahedral smectite clay particles characteristic of the FEBEX reference sample. The possibilities that explain these peaks are: 1) the presence of illite/smectite mixed layers (I/S ML), because illite has a trans-vacant configuration, 2) the presence of other type of clay mineral mixed layer, such as Chl/S ML, 3) a mixing of smectite particles with high-iron and aluminous varieties, since the presence of iron at octahedral sites induces a decrease of the dehydroxylation peak towards 450–520 °C, as occurs in nontronites (the main smectite types exhibit different dehydroxylation temperatures: 450–520 °C for dioctahedral Fe-smectites (trans-vacant); 670–730 °C for dioctahedral Al-smectites (cis-vacant) and 770–860 °C for trioctahedral Mg-smectites, octahedral cations determining the dehydroxylation temperature), 4) a change of the smectite structure, with an increase of octahedral OH groups at trans-vacant positions (and hence more tetrahedral charge), instead of being most of them at cis-vacant positions as occurs in the FEBEX reference sample, 5) a change in the smectite structure with the presence of two types of smectite particles: those with mainly tetrahedral substitutions (beidellitic type) and those with mainly octahedral substitution (montmorillonite type), 6) crystal

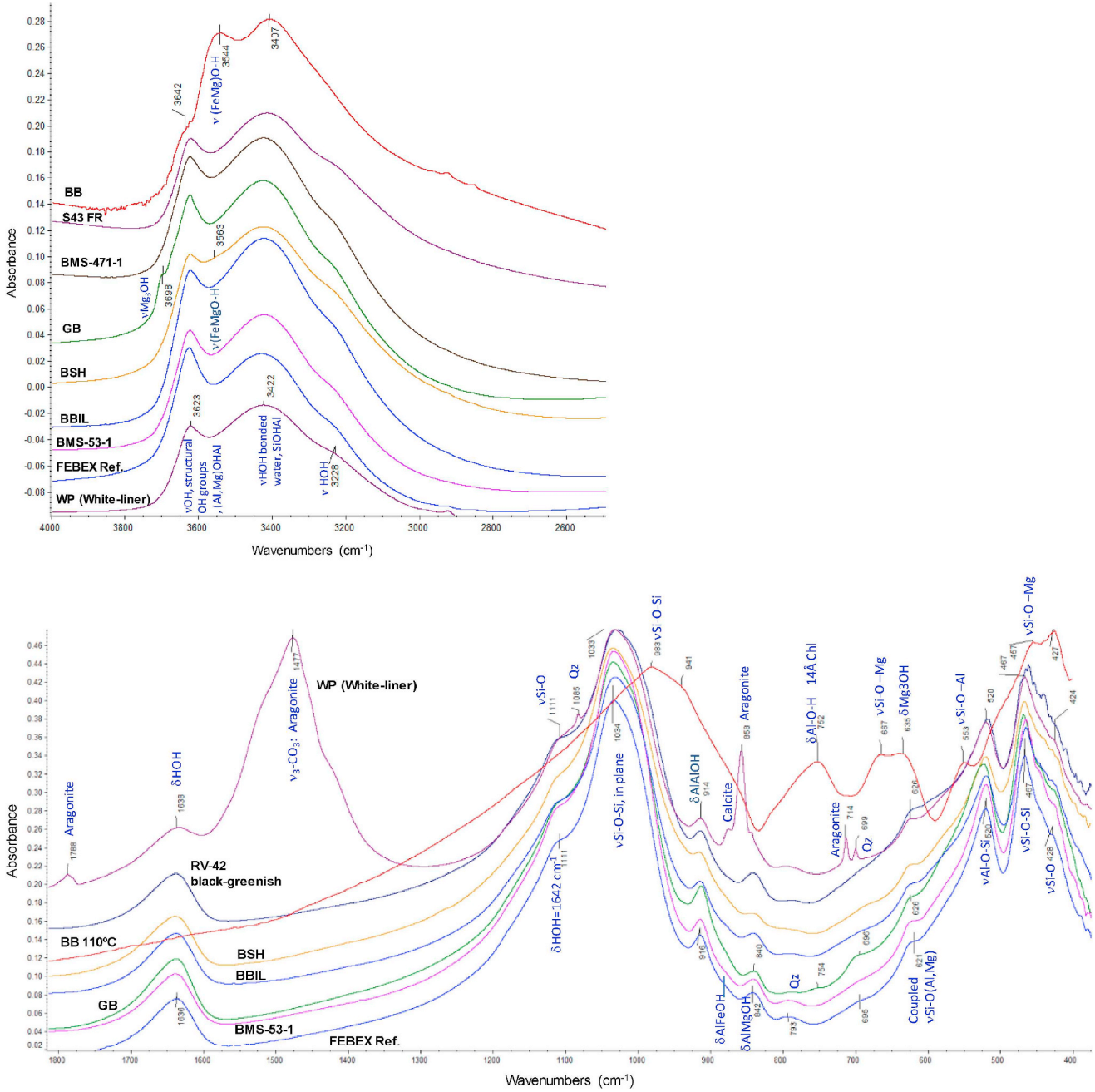

Fig. 4. FTIR spectra (OH-stretching and OH-bending regions) from samples taken above (BMS) and inside the liner (protrusions) at contact with the Heater #2.

structure changes as result of Fe(III) reduction in order to accommodate the larger size of Fe(II) and increased negative charge, which generate partial dehydroxylation and loss of structural OH groups (Stucki and Roth, 1977), and 7) structural transformations of the cv 2:1 layers, which were dehydroxylated due to heating or another process, such as Fe(III) reduction. This process involves not only the loss of hydroxyls but also the migration of Al cations into vacant sites in a portion of the sample. Thus, after rehydroxylation (e.g., cooling in water vapor) a cv montmorillonite transforms to a mixture of two montmorillonites one having tv and the other cv 2:1 layers (Drits et al., 1995; Emmerich et al., 1999).

The retrieved samples show, in turn, a variation in the temperature of the decomposition/recrystallization peak. The associated endothermic peak located around 867 °C in the reference sample shifts to lower temperatures (up to 845 °C). Indeed, there is a modification in the shape and magnitude of the high temperature endothermic-exothermic peak between 850 and 1000 °C. The exothermic peak also shifts from 1010 °C in the reference sample to a higher exothermic peak at a lower temperature around 985 °C (Fig. 5). This is well observed when the < 2 μm fraction is analysed (Fig. 6). In this fraction the peak between 592 and 622 °C is not detected (maybe because of the low content, being overlapped within the width peak at 650 °C, or the particle size), but the additional dehydroxylation peak around 550 °C is well distinguished and associated with a modification in the high temperature endothermic-exothermic decomposition peak between 850 and 1000 °C (Figs. 6 and 7). The magnitude of the exothermic peak is intensive in the case of a smectite with high Mg content, and decreases or disappears in the case of high Al or Fe content, i.e., this peak increases in height when Mg increases, and decreases in temperature when Mg decreases. In this case, the sharp exothermic peak indicates a higher Mg content at octahedral sheets in the samples at contact with the heater, as observed from the < 2 μm fraction in the BMS samples in Section 47

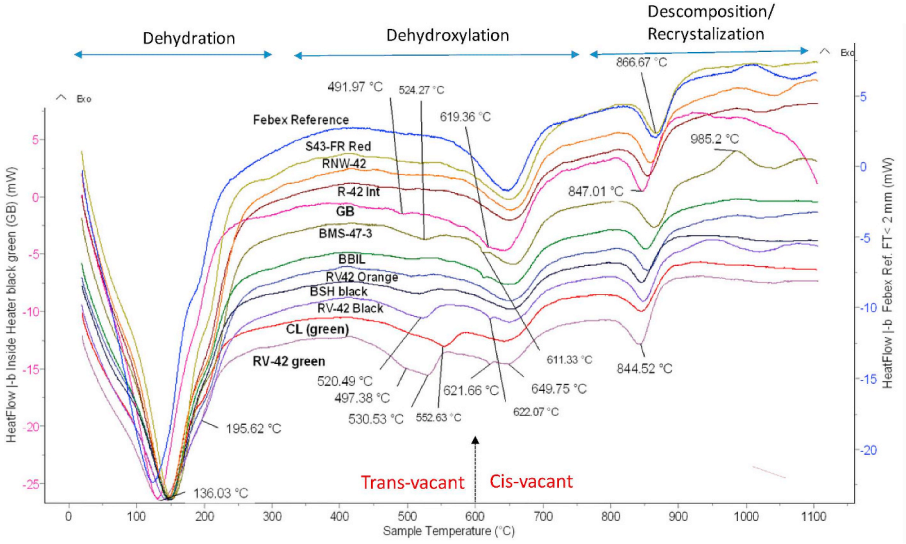

Fig. 5. Comparison of DSC curves from the bulk bentonite samples (total fraction): at direct contact with the liner (BMS-47-3) and protrusions through the liner holes towards the heater.

and Section 53 (Fig. 6), and in the GB protrusion sample (Fig. 7). The presence of the sharp exothermic-endothermic peak is observed in all BMS samples but not in all the protrusion samples. This depends on the type of sample, missing for example in the protrusion samples with apparently a lower degree of alteration (RNW-42 black&white) or showing a reddish color (BBIL-42, S-43 FR red); and found in the GB and RV-42 black-greenish samples. These latter samples have a higher Fe^{2+} content (see below). It should be taken into account that the protrusion samples were collected *on site* by CIEMAT and BGR, and only the CIEMAT samples were preserved immediately in Al-foil bags, preserving the redox state of the samples. Maybe this is the reason because the double dehydroxylation peak is only observed at CIEMAT samples.

More interesting is that in the samples with abnormal behaviour, i.e., having two dehydroxylation peaks around 550 °C and 650 °C, a slight mass change is observed in the dTG curves at 835–850 °C (Figs. 6 and 7). This is mandatory and restricted to trioctahedral smectites. Therefore, a modification of the smectite clay mineral structure from the reference dioctahedral to a trioctahedral character is inferred in the samples at close contact with the Heater#2. From possible trioctahedral clay minerals, only saponite shows a dehydroxylation peak around 850–900 °C with a mass change in this peak. Chlorites or Chl/S MLs do not show mass changes at this temperature. Therefore, different types of clay mineral particles are in these samples: 1) the double dehydroxylation peaks at 550 °C and 650 °C indicate the presence of two types of smectite particles, those with tetrahedral substitutions (550 °C), and hence trans-vacant positions, and those with octahedral substitutions (650 °C), supported by the crystallochemistry of the clay particles analysed by TEM and SEM (see below), so the increase of iron at octahedral sites may be ruled out, 2) the mass change in the dTG curves at 835–850 °C indicates the presence of trioctahedral smectite (saponite), and 3) the peak around 620 °C may be indicative of the presence of interstratified smectite particles (e.g., I/S MLs, Chl/S MLs, ...). Finally, chlorite was also identified by TG-DSC in the black ball (BB) sample, located at the frontal part of Heater #2 (Supplementary Fig. S8), showing a dehydroxylation peak at 589 °C and an exothermic peak at 948 °C with no mass variation at this temperature.

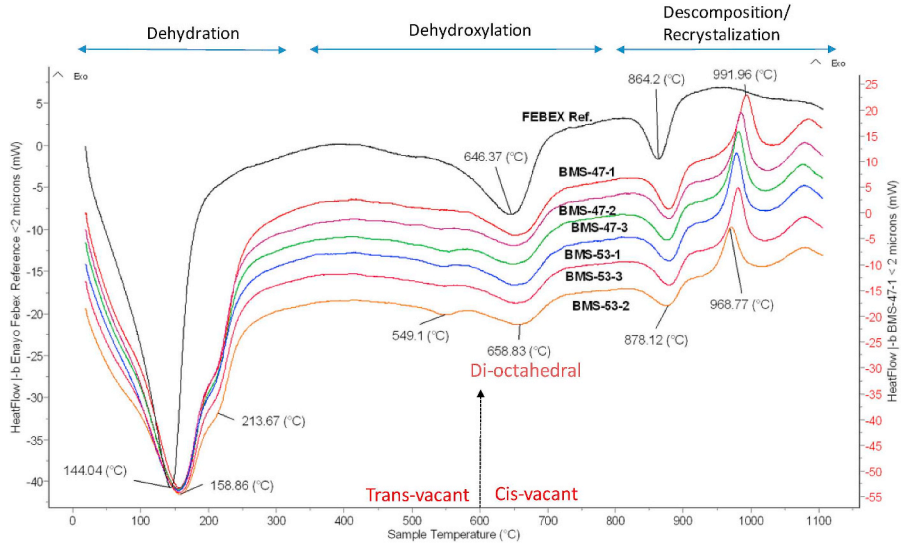

Fig. 6. Comparison of DSC curves from the samples BMS-47-xx and BMS-53-xx (< 2 μm fraction) at direct contact with the liner.

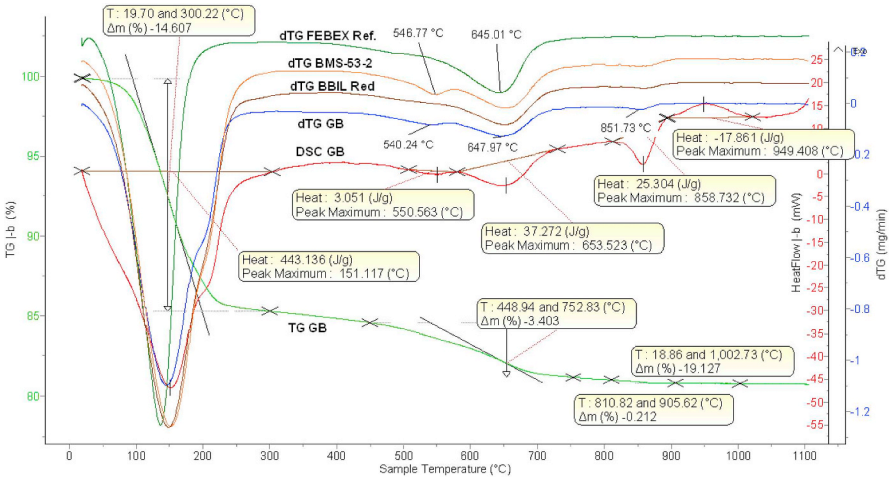

Fig. 7. TG-DSC curves from the GB-42 bentonite protrusion sample through the liner holes towards the heater. dTG curve is compared with dTG curves from other < 2 μm fraction samples: FEBEX reference, BBIL red (protrusion) and BMS-53-2 (above the liner). (For interpretation of the references to color in this figure legend, the reader is referred to the Web version of this article.)

Table 2
Major mineral phases and accessory minerals observed by SEM in the samples at contact with the liner (BMS) and in the protrusions (in cursive: present in the reference sample).

Mineral phases	Section 47 and Section 54	Protrusions
Ca-carbonates	BMS-47-1	WB-42; PS-43; RNW42; RV-42 GB-42; BPB
Dolomite	–	PS-57; RNW42
Fe-carbonates	–	BBIL-42; PS-43; PS-43 Red; RNW42; BSH-42; GB-42
Ca-sulfates	BMS-47-2	BBIL-42; WB-42; PS-57; RNW42 RV-42; GB-42
Ba(Sr)-sulfates	BMS-47-1 BMS-47-2	BBIL-42; WB-42; PS-43; PS-43 Red; RV-42; GB-42
Fe-sulfides	–	RV-42
PbS	–	PS-43
Fe-oxides	BMS-47-2	BBIL-42; WB-42; PS-43 PS-43 Red; BSH-42; GB-42; BPB
Fe–Ti–Mn-oxides	BMS-47-2	WB-42; PS-57; PS-43 Red; RNW42; BPB
Ilmenite	BMS-47-1	BBIL-42; RNW42; RV-42
Hg particles	–	WB-42; PS-43; PS-57 Red; RV-42
Zircon	–	RNW42; RV-42; BSH-42
Xenotime	BMS-47-1	
Monazite	–	RNW42; GB-42; BPB
Apatite	BMS-47-2	PS-43; BSH-42; GB-42
Silica	BMS-47-1 BMS-47-2	WB-42; PS-43; PS-43 Red RNW42; RV-42; GB-42; BPB
Plagioclases	BMS-47-1 BMS-47-2	BBIL-42; WB-42; PS-43 PS-43 Red; RNW42; RV-42; BSH-42; GB-42; BPB
K-Feldspars	BMS-47-1	RNW42; BSH-42; GB-42; BPB
Biotite	BMS-47-1 BMS-47-2	BSH-42
Organic matter (OM)	BMS-47-1 BMS-47-2	WB-42; PS-43; PS-43 Red RNW42; BSH-42; GB-42; BPB
C, N	–	PS-43
Cl	BMS-47-1 BMS-47-2	BBIL-42; WB-42; PS-43; PS-43 Red; RNW42; BSH-42; GB-42
Smectite	BMS-47-2	PS-43; RNW42; RV-42 BBIL-42; BSH-42; GB-42; BPB
Brucite or Mg-rich clay mineral	BMS-54-5B-1	
Nontronite/Fe-rich type with ↑K	–	S43FR red particles
Chlorites	–	BSH-42; BPB; BB
Kaolinite?	–	GB-42

4.1.4. Scanning electron microscopy (SEM) analysis

The aims of the SEM analyses were to analyse the main and accessory minerals in the bentonite, as well as the microstructure and crystallochemistry of the clay minerals. The results are summarised in Table 2.

The major mineral phases are smectite, quartz and feldspars. In general, the accessory minerals of the FEBEX bentonite are: carbonates, sulfates, zircon, monazite, biotite, muscovite, ilmenite and apatite, which were also found in the retrieved samples. However, other accessory minerals were identified, which correspond to iron-bentonite interactions at the liner/Heater#2 contact, i.e., to corrosion by-products, such as: Fe-oxy/hydroxides, sometimes impregnated with Cl (Supplementary Fig. S15), Fe-carbonates (Supplementary Fig. S16), calcite and dolomite (Supplementary Fig. S17), pyrite and sulfates (Ca- and Ba–Sr-sulfates) (Supplementary Fig. S18), silica (Supplementary Fig. S19) and organic matter with nitrogen (see Fernández et al., 2018 for additional information). Furthermore, apart from smectite, other types of clay minerals were found, such as nontronite/Fe-rich smectite with high K content and chlorites (Supplementary Fig. S20).

4.1.5. Transmission electron microscopy (TEM) analysis

TEM was used for examining the morphology of the platy clay particles and/or clay aggregates, and analysing the crystal chemistry of the clay minerals and possible alterations. TEM images from some retrieved samples are shown in Supplementary Fig. S21. The structural formulae calculated from EDS-analyses on clay mineral particles (as average of 5–11 point analysis) are shown in Table 3, the composition being quite homogenous. Most of them correspond to montmorillonite type smectites, as in the reference FEBEX bentonite. This is in agreement with further bentonite analyses performed on samples taken from different sections throughout the bentonite barrier (Fernández et al., 2018). However, some significant variations were observed in some clay particles, which were related with changes in the cation composition at tetrahedral sheets (increasing the tetrahedral charge), slight increase in magnesium at octahedral sheets, and increases in the layer charge above 0.6 eq/h.u.c., which is the limit for typical smectites (Fig. 8). With respect to iron content at octahedral sheets, taken as Fe (III), it increases in the protrusion samples, where apart from montmorillonite particles, other types of clay minerals were found (Table 3): nontronite (dioctahedral smectite with mainly tetrahedral substitutions), Fe-rich chlorites (tri(-di)octahedral chlorite), and illite in a sample from the bentonite block BB-47-9 close to liner contact.

4.2. Geochemical analysis

The geochemical analysis of the samples consisted of chemical analyses of the main elements in the total fraction by XRF

Table 3
Structural formulae of clay mineral particles detected in the samples at contact with the liner/heater and in the protrusions.

Sample	Structural formula	Layer charge (eq/ h.u.c.)	Σ_{tet}	Σ_{oct}	τ charge (%)	O. charge (%)	Weight (g/mol) p.f.u.
FEBEX Ref. [5]*	$(Si_{3.93}Al_{0.07})^{IV}$ $(Al_{1.43}Fe^{3+}_{0.15}Mg_{0.49}Ti^{4+}_{0.01})^{VI}$ $O_{10}(OH)_2$ $(Ca_{0.02}Na_{0.24}K_{0.05})_{0.30}$	0.32	4.0	*2.08*	21	79	747.29
	$(Si_{3.93}Al_{0.07})^{IV}$ $(Al_{1.43}Fe^{3+}_{0.15}Mg_{0.41}Ti^{4+}_{0.01})^{VI}$ $O_{10}(OH)_2$ $(Ca_{0.02}Mg_{0.08}Na_{0.24}K_{0.05})_{0.38}$	0.48	4.0	*2.00*	14	86	747.29
BMS-47-2 [13] *montmorillonite*	$(Si_{3.76}Al_{0.24})^{IV}$ $(Al_{1.30}Fe^{3+}_{0.15}Mg_{0.50}$ $Ti^{4+}_{0.03}$ $Mn^{2+}_{0.02})^{VI}$ $O_{10}(OH)_2$ $(Ca_{0.17}Mg_{0.08}Na_{0.17}K_{0.06})_{0.48}$	0.73 (0.57)	4.0	2.00 (2.08)	33 (42)	67 (58)	758.70
BMS-53-2 [5] *montmorillonite*	$(Si_{3.98}Al_{0.02})^{IV}$ $(Al_{1.43}Fe^{3+}_{0.01}Mg_{0.56})^{VI}$ $O_{10}(OH)_2$ $(Ca_{0.02}Mg_{0.25}$ $Na_{0.02}K_{0.02})_{0.31}$	0.57 (0.08)	4.0	2.00 (2.25)	3 (22)	97 (78)	734.40
RV-42 Green [7] *montmorillonite*	$(Si_{3.82}Al_{0.18})^{IV}$ $(Al_{1.19}Fe^{3+}_{0.22}Mg_{0.57}Ti^{4+}_{0.01})^{VI}$ $O_{10}(OH)_2$ $(Ca_{0.08}Mg_{0.27}K_{0.06})_{0.41}$	0.76 (0.22)	4.0	2.00 (2.27)	24 (85)	76 (15)	754.82
Liner Red (BBIL-42) [6] *montmorillonite*	$(Si_{3.85}Al_{0.15})^{IV}$ $(Al_{1.29}Fe^{3+}_{0.32}Mg_{0.37}Ti^{4+}_{0.01})^{VI}$ $O_{10}(OH)_2$ $(Ca_{0.13}Na_{0.01}Mg_{0.11}K_{0.03})_{0.28}$	0.52 (0.31)	4.0	2.00 (2.11)	29 (49)	71 (51)	756.31
Heater Black (BSH) [5] *montmorillonite*	$(Si_{3.75}Al_{0.25})^{IV}$ $(Al_{1.60}Fe^{3+}_{0.01}Mg_{0.39})^{VI}$ $O_{10}(OH)_2$ $(Ca_{0.03}$ $Mg_{0.20}Na_{0.15}K_{0.05})_{0.42}$	0.65	4.0	2.00	39	61	741.18
Liner Red (BBIL-42) *Nontronite*	$(Si_{3.11}Al_{0.89})^{IV}$ $(Al_{0.25}Fe^{3+}_{1.74}Mg_{0.01})^{VI}$ $O_{10}(OH)_2$ $(Ca_{0.10}Mg_{0.34}K_{0.02})_{0.46}$	0.90	4.0	2.00	99	1	844.98
P. Black (BB) [7] *Chlorite Fe-rich*(**)	$(Si_{2.91}Al_{1.09})^{IV}$ $(Fe^{2+}_{2.61}Mg_{0.14}Mn^{2+}_{0.080.17})^{VI}$ $O_{10}(OH)_2$ $(Ca_{0.02}Na_{0.01}K_{0.01})_{0.04}$ $[Al_{1.37}Mg_{1.63}(OH)_6]$	0.06	4.0	3.00	–	–	–
P. Black (BB) [7] *Chlorite Fe-rich*(***)	$(Si_{2.95}Al_{1.05})^{IV}$ $(Fe^{3+}_{0.38}Fe^{2+}_{1.90}Mg_{0.22}Mn^{2+}_{0.080.42})^{VI}$ $O_{10}(OH)_2$ $(Ca_{0.02}Na_{0.01}K_{0.01})_{0.04}$ $[Al_{1.43}Mg_{1.57}(OH)_6]$	0.06	4.0	3.00	–	–	–

* In square brackets: number of point analyses performed for calculating the average structural formula. Smectite structural formula calculated by fixing the sum of octahedral cations at 2.0, except in the first row (FEBEX ref.). The data given in parentheses are those calculated without fixing the sum of octahedral cations at 2.0.

** Total Fe as Fe(II).

*** Previous structural formula but considering the % of Fe(II) and Fe(III) determined in Section 4.2: Fe(II) = 92.7%; Fe(III) = 7.3%.

(Supplementary Fig. S22, Table S2), and total carbon and sulfur content by combustion. The Fe speciation (Fe(II)/Fe(III)) in the bentonite material was analysed both in the BMS material and in the protrusion samples (Table 4) via NH_4HF_2—H_2SO_4 leaching tests (see Section 3.3.3).

It is interesting to note the increase of magnesium and the decrease of sodium in the samples close to the liner/Heater#2 (Supplementary Fig. S22), calcium remaining constant except in the samples which were mainly carbonates (E6, E7 and E8). Iron content increases mainly in some protrusion samples (Supplementary Table S2) where oxy-hydroxides were neoformed. Carbon content is mainly as inorganic carbon, increasing in some protrusion samples, where carbonates were precipitated (Supplementary Table S3). Organic carbon is always close or below the detection limit, except in the protrusion sample E8, whose value changed from 0.06% to 0.20%.

The presence of Fe(II) in the bentonite samples is of interest for knowing redox processes inside the bentonite buffer. The results are shown in Table 4 and compared with the values obtained from FEBEX reference sample. An increase in total iron is observed in the protrusion samples with respect to the reference value and the retrieved BMS samples. Fe(III) is the main iron species in the samples, indicating a high degree of oxidation, but some amount of Fe(II) is observed, ranging from 0 to 2 wt.% in the BMS samples and from 3 to 18 wt.% in the protrusion samples, being of 7 wt.% in the FEBEX reference. Thus, higher values of Fe(II) than in the reference sample are observed mainly in the protrusion samples: CL, RV-42, RN-42, BSH-42, GB-42 and S43-FV, with values ranging from 0.31 to 0.64 wt.%. Fe(II) may be from the clay mineral structure and from magnetite. However, it should be taken into account that the magnetized particles were discarded from the samples before analysis, so this Fe(II) is supposed to be mainly from the smectite structure. However, the increase of Fe(III) in the samples, from 2.51 wt.% (CL) to 5.30 wt.% (BBIL or S43-FV) with respect to the reference sample (2.15 wt.%) may indicate also the presence of non-magnetic iron oxy-hydroxides, such as goethite as observed in DRX and FTIR analyses, or an increase of Fe(III) in the clay particles. It is interesting to note the lower amount of Fe(II) in the BMS samples (from above the liner), which are practically oxidized, with respect to the protrusion samples (from inside the liner). The Fe speciation in the BB sample (chlorite) is 93% as Fe(II) and only 7% as Fe(III).

4.3. Physico-chemical properties

The cation concentration at exchange sites and CEC values are shown in Fig. 9 (see also Supplementary Table S4). CEC values seem to decrease in the bentonite samples close to the Heater#2 contact (from 98 meq/100 g in reference value to 86-64 meq/100 g in sample BMS-53-2), representing a 11–35% lower than the reference value. The lowest values obtained between 38 and 60 meq/100g correspond to the samples E6, E7 and E8, analysed by BGR, which are mainly composed by carbonates, having a lower smectite content. A clear decrease of sodium and an increase of magnesium and calcium at exchange sites are observed in the BMS and protrusion samples with respect to the reference FEBEX sample, potassium slightly increasing from 2.9 meq/100g (reference) to a maximum value of 3.4 and 4.0 meq/100g for CIEMAT and BGR samples, respectively. However, the magnesium at interlayer sites maybe overestimated, as detected by the difference in the CEC values and the sum of exchangeable cations. This is due to the high salinity of the samples close to the liner/Heater#2 contact (see below). In the determination of exchangeable cations, only sodium and calcium concentrations were corrected from the soluble salts present in the solid phase.

From 1:4 aqueous leaching tests, a sharp increase in salinity and in the Cl, Na, Mg, Ca and K contents, as well as a decrease of bicarbonates are observed in the samples with respect to the rest of reference sample (Fig. 10 and Supplementary Table S5), indicating that the hydration front saturating the bentonite barrier from the granite surrounding formation reached until the inner part of the barrier, the salts being

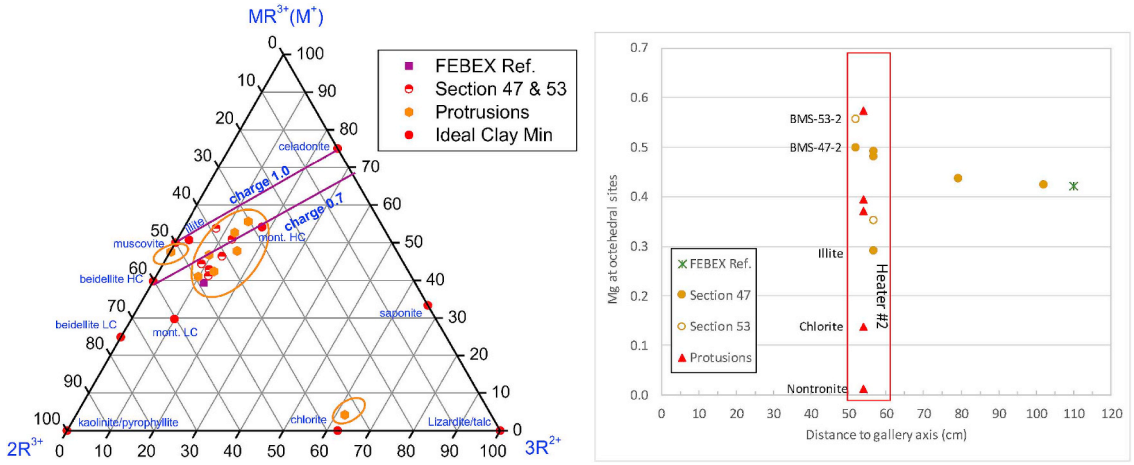

Fig. 8. a) Solid solution projection in the MR^{3+}-$2R^{3+}$-$3R^{2+}$ system of the retrieved samples, b) magnesium at octahedral sites as a function of the distance to the gallery determined by TEM analysis.

Table 4
Total Fe, Fe(II) and Fe(III) in the bentonite samples at contact with the liner at sections S47 and S53 and in protrusion samples.

Sample	w.t.% Fe_{total} average	w.t.% Fe(II) average	w.t.% Fe(III) average	Sample	w.t.% Fe_{total} average	w.t.% Fe (II) average	w.t.% Fe(III) average
FEBEX Ref.	2.30	0.15 (7%)	2.15	CL	3.05	0.54 (18%)	2.51
BM-S-47-1 white	1.84	0.04 (2%)	1.80	RV-42	3.65	0.48 (13%)	3.17
BM-S-47-1 red	2.00	0.05 (2%)	1.95	RN-42	4.68	0.31 (7%)	4.38
BM-S-47-2 white	1.77	0.03 (1%)	1.74	RI-42	2.12	0.08 (4%)	2.04
BM-S-47-2 red	2.17	< 0.02 (0%)	2.17	RNW-42	3.07	0.06 (2%)	3.01
BM-S-47-3 white	1.84	0.06 (3%)	1.78	RO-42	1.60	0.09 (6%)	1.51
BM-S-47-3 red	2.35	< 0.02 (0%)	2.35	BSH-42	3.09	0.27 (9%)	2.82
BM-S-53-1	2.15	0.04 (2%)	2.11	BBIL-42	5.43	0.13 (2%)	5.30
BM-S-53-2	2.58	0.03 (1%)	2.55	BBL-42	5.03	0.11 (2%)	4.92
BM-S-53-3	2.21	0.01 (0.4%)	2.19	WB-42	1.87	0.06 (3%)	1.81
				GB-42	3.91	0.64 (16%)	3.27
				S43-FV	5.63	0.34 (6%)	5.29
				BB	24.5	22.7 (92.7%)	1.80

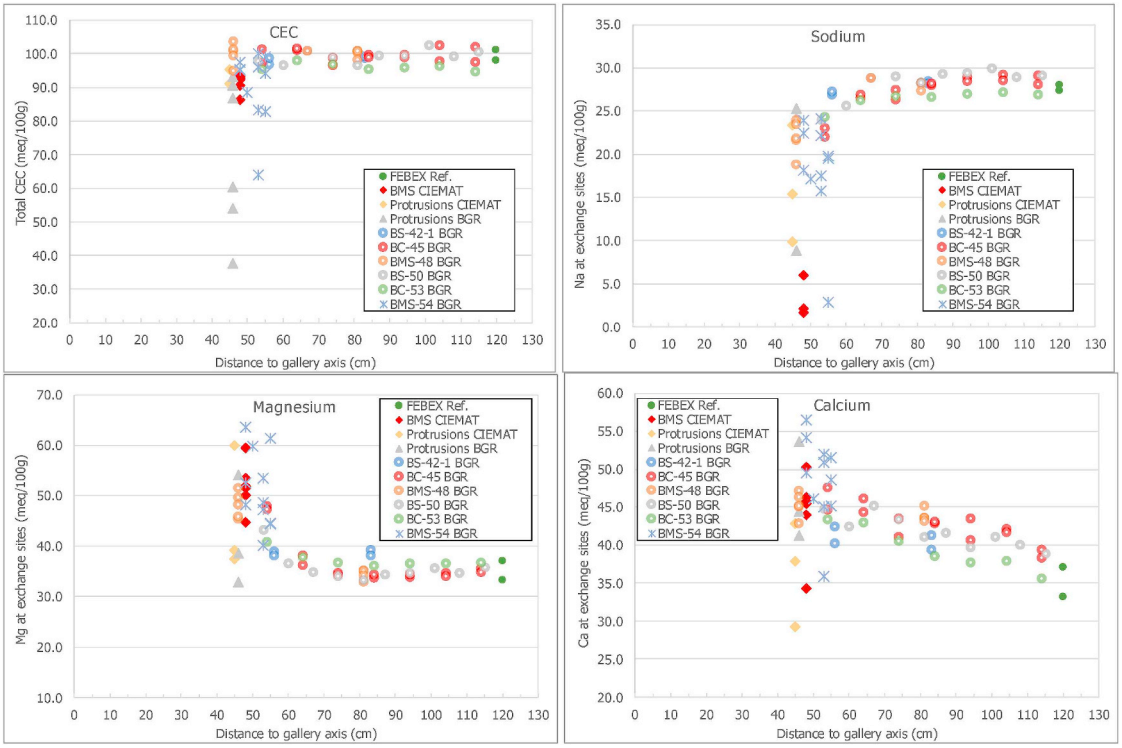

Fig. 9. Total CEC and sodium, magnesium and calcium content at exchange sites (in meq/100g) as a function of the distance to the gallery axis from BMS and protrusion samples at contact with the liner/Heater#2.

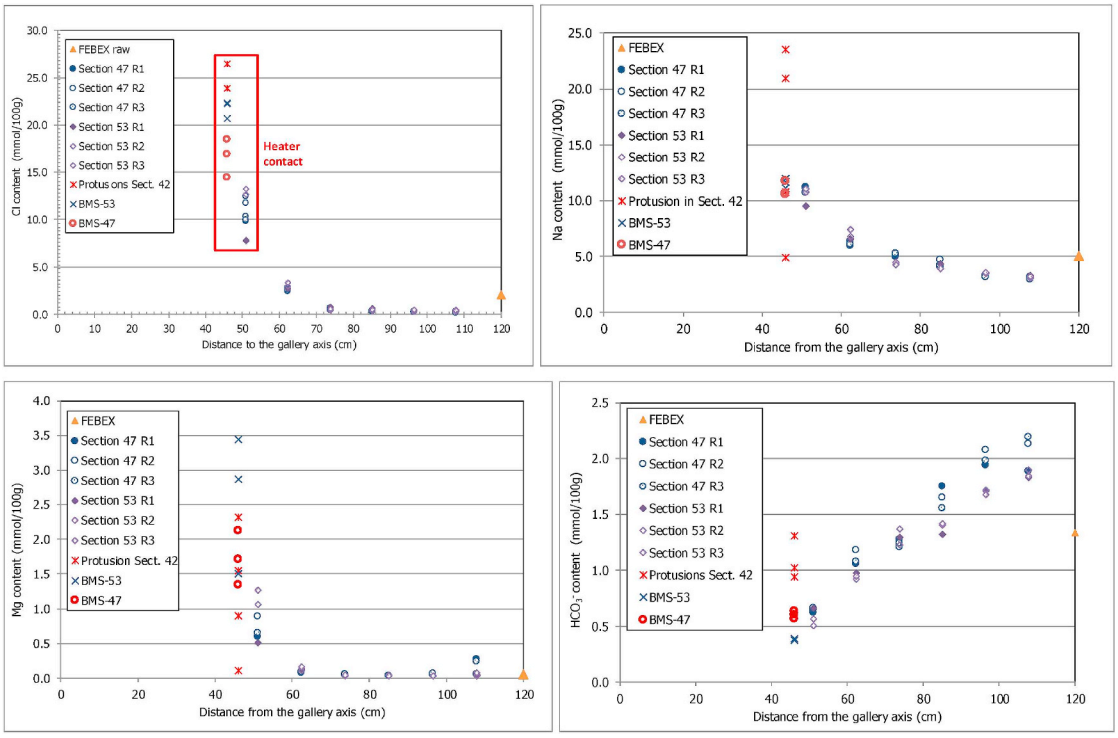

Fig. 10. Chloride, sodium, magnesium and total alkalinity (as bicarbonate) obtained from 1:4 aqueous leaching as a function of the distance to the gallery axis from BMS and protrusion samples at contact with the liner/Heater#2.

transported with water probably an advection(-diffusion) process. This can be observed when the data are compared with other samples from Section 47 and Section 53 along the whole bentonite barrier from granite contact to Heater#2 contact (Fig. 10). The decrease of bicarbonates in the samples at Heater#2 contact indicates the precipitation of Ca-carbonates, as observed in the mineralogy of some samples. The high amount of chlorides, sodium and magnesium imply the high salinity close to the heater, where due to the low water content (< 18%) and heat, the precipitation of halite and other Mg—Cl salts in some zones is possible. Furthermore, the possible presence of Mg—Cl ion parings is inferred with these high concentrations, which may enter into interlayer sites. More interesting is the presence of volatile fatty acids, VFAs, or carboxylic acids, such as acetate, formate and oxalate in the aqueous extracts (Supplementary Table S5), which are related with the corrosion process and subsequent degradation/oxidation of organic matter (see below). Thiosulfate ($S_2O_3^{2-}$) was found in the protrusions samples BBIL and BHS. An increase of silica from 12 mg/L to 56 mg/L was detected in the sample S43 FR red.

A clear decrease of the BET surface area is observed in the retrieved bentonite samples as a function of the Heater#2 contact (from 59 to 21 m^2/g). This decrease is observed not only in the BMS samples (at external contact of the liner) and protrusion samples (at close contact with the Heater#2) but also in the inner bentonite block of the Section 47 (BB-47-9) (see Supplementary Table S6).

5. Discussion

During 18 years of heating and hydration in the FEBEX *in situ* test, physico-chemical, geochemical and mineralogical alterations of the bentonite could have produced a redistribution and neoformation of mineral phases, dissolution processes, changes in total adsorption capacity (CEC) and crystallochemical changes in the smectite that could have affected the physico-chemical and mechanical properties of the bentonite. Some specific reactions observed in laboratory and large-scale experiments were also observed in the FEBEX *in situ* experiment. However, specific results were obtained from this FEBEX *in situ* experiment, the longest real scale *in situ* experiment up to date.

5.1. Dissolution/precipitation processes

Dissolution and precipitation processes were mostly restricted to partly soluble minerals, such as carbonates and sulfates, and depended on the evolution of the pore water chemistry through the bentonite barrier. The initial compacted bentonite, with a water content of 14% and 1.60 g/cm^3 of dry density after emplacement, evolved towards a fully saturated system after 18 years of experiment, except in the blocks located at the Heater#2 contact, where the saturation degree was around 85–92% (Villar et al., 2016). During the infiltration of the surrounding granitic groundwater, the soluble salts of the bentonite were transported towards the inner part of the barrier by probably an advective(-diffusive) transport (Fig. 10), modifying the pore water chemistry, the composition of the cations at exchange sites and the mineral equilibria.

The initial bentonite pore water was Na—Mg—Cl—SO_4 water-type with ~0.3 M ionic strength (I), whereas the granitic groundwater was a diluted and reducing water (E.C. < 100 µS/cm, Eh −200 mV, I = 0.001 M), pH close to 9, Na-Ca-TIC-F water-type. Chlorides were transported with water during the saturation process of the bentonite, which depended on the water gradient/suction of the bentonite rather than on the hydraulic pressure of the granitic rock (0.72 MPa). The pore water composition extracted by squeezing from bentonite blocks changed to Na—SO_4—Cl water-type and I = 0.04 M at the granite interface and to Na—Mg—Ca—Cl water-type and I = 0.41 M at the heater contact (Fernández et al., 2018). The maximum content of chlorides after 18 years of experiment was observed at the contact of Heater #2 (Fig. 10). Other non-conservative ions such as carbonates and sulfates were transported more slowly because they were involved in dissolution/precipitation processes in the bentonite. Precipitated Ca-carbonates and Ca-sulfates (probably as anhydrite due to the temperature at liner/Heater#2 contact: > 93 °C), were widely observed in all sections of the bentonite buffer by SEM, but were particularly observed at the liner/Heater #2 interface (Supplementary Fig. S17, Fig. S18b).

Anhydrite was detected by FTIR in a sample close to the Heater#2 (Fernández et al., 2018).

Increases of silica may be due to either a dissolution process of the clay minerals or to the effect of heating that provokes the dissolution of SiO_2 with the subsequent re-precipitation in cooler areas and possible cementation of pores. Increases of quartz and/or silica were observed by XRD in some samples, such as RV-42 green and BSH black (Fig. 3) and by SEM (Supplementary Fig. S19); whereas dissolution of cristobalite and feldspars, was not detected. However, an increase of dissolved silica was detected in the aqueous extracts in the protrusion sample SR43 FV red, as indicated in Section 4.3. Dissolution of cristobalite and zeolites was found in the ABM experiment (Kaufhold et al., 2013).

5.2. Cation exchange reactions

Apart from dissolution/precipitation processes, the most significant changes observed in the FEBEX *in situ* test after 18 years of experiment were the cation concentrations at interlayer sites throughout the bentonite barrier (see Fernández et al., 2018).

Cation exchange reactions may be enhanced by temperature and by dissolution/precipitation processes during the saturation of the bentonite barrier. In the FEBEX *in situ* experiment the temperature was 100 °C but relatively few water was available (w.c. ≤ 18% close to Heater #2 contact). Nevertheless, modifications in the cation exchange population were observed. Exchangeable Mg and Ca increased towards the heater while Na decreased (Fig. 9), as observed both from the cation exchange composition and from XRF analyses of the total solid phase (Supplementary Table S2). Potassium slightly increased or remained constant at the Heater #2 contact changing the values from 2.9 meq/100g (reference) to a maximum 3.4–4.0 meq/100g. Mg from pore water obviously moved towards the heater together with other soluble ions, which at the same time explains the Mg accumulation near the Heater #2. The possible presence of $MgCl^+$ ion pairs, which may occupy interlayer sites, may explain the higher mobility and higher amount of Mg than calcium at exchange sites in some samples, Ca being involved, in turn, in the precipitation of Ca-carbonates and Ca-sulfates at the heater contact (Supplementary Fig. S16, Fig. S17), and in the decrease of alkalinity values from aqueous extracts (Fig. 10). It should be taken into account that Mg content at exchange sites was not corrected from contents in soluble salts, so exchangeable Mg may be overestimated because its association with sulfates, carbonates (dolomite) and $MgCl_2$ soluble salts. What it is clear is the decrease of Na at exchange sites, initially with a 33% in the reference bentonite and decreased up to a 9% at the Heater#2 interface. However, the sink of sodium could not be identified yet, probably because of the low amount and the respective detection limits of both XRF and XRD. However, high concentrations of sodium and magnesium were detected in the pore waters close to the Heater#2 contact, and the presence of NaCl and $MgCl_2$ salts due to evaporation at the heater interface has to be considered. In addition, organics were detected in the pore water samples close to the heater interface, and some type of association with sodium cation cannot be ruled out; e.g., as sodium oxalate and/or sodium acetate.

5.3. Metal corrosion and hydrocarbons generation: driving force for redox buffering and mineralogical changes

In real repository conditions, after a transient period, the system is supposed to be water saturated, anoxic and slightly reducing. Under these conditions, it is expected that anoxic corrosion of canisters takes place. In the FEBEX *in situ* test only 85–92% of water saturation was achieved at the Heater#2 contact after 18 years of experiment. Real anoxic conditions with dissolved O_2 values below $1{\cdot}10^{-3}$ mmol/L were never reached, the minimum measured O_2 contents accounted for about $2{\cdot}10^{-2}$ mmol/L after 1.5 years of switching on the heaters; i.e. the system was not gas-tight, and there was an ingress of O_2 during the experiment over time (Fernández, 2018; Fernández et al., submitted). Metal corrosion was represented by a corrosion layer on the surface of the liner/Heater #2 with maximum thicknesses of 180–350 μm and depths of 110–190 μm (Wersin and Kober, 2017), an increase of the Fe-content in bentonite samples taken from the first mm from the liner/Heater #2 contact, increasing the values from 3.1 wt.% to 6–19 wt.% (Supplementary Fig. S22, Table S2); and the presence of corrosion products. A range of Fe-oxyhydroxides were detected, the most prominent being goethite, hematite and magnetite (Table 1, Fig. 3a, Supplementary Fig. S15). In addition, during dismantling, the bentonite close to the liner/Heater#2 contact presented different colors: pale-yellowish (reference), brown-reddish, green and black, which implies different redox stages, the latter two being representative of anoxic/anaerobic conditions with presence of Fe(II). Therefore, although most of the corrosion products resulted from oxic corrosion, localized or partially reduced conditions were achieved inside the bentonite barrier.

The description of the redox evolution in the bentonite buffer may be based on the corrosion products detected because metal corrosion is one of the main processes affecting the redox state (Duro et al., 2014). However, the gas and water evolution allows also to describe the redox system inside the barrier (Fernández et al., 2018). The initial stages of the FEBEX *in situ* test occurred at oxic conditions due to the residual air in the unsaturated bentonite material, and the gaps between bentonite blocks and the liner/Heater#2. The corrosion of the C-steel Heater #2 and other metals produced oxygen depletion and, as consequence, the precipitation of Fe(III) oxides and hydroxides (ferrihydrite, goethite and hematite).

After oxygen consumption, metals corrode in the absence of oxygen, under anoxic conditions. Since Fe(s) is thermodynamically unstable in water, in absence of any other oxidant, metals corrode through water reduction, with subsequent hydrogen generation and the formation of ferrous hydroxide, which evolves towards the formation of magnetite, in the so-called Schikorr reaction (e.g. Wersin et al., 2007). Magnetite was the reduced iron oxide corrosion product detected in the samples close to the liner/Heater #2 contact, hydrogen being detected and monitored along the 18 years of the FEBEX *in situ* test (Fernández, 2018; Fernández et al., submitted).

However, the presence of hydrogen, methane and other reduced saturated hydrocarbons when oxygen was present at the beginning of the test and also over time, due to no gas-tight conditions, indicated another possible reaction. This reaction is related with the corrosion and hydrolysis of carbon-containing steels, liner and heater through a similar Fischer-Tropsch (FT) synthesis reaction using iron as catalyst, yielding a mixture of H_2, CO, CO_2, alkanes, alkenes and oxygenated organic compounds (Wieland and Hummel, 2015; Cataldo, 2003). This reaction was corroborated by the monitoring of these compounds over the 18 years of experiment (Fernández, 2018), and because the cross plots of $\delta^{13}C{-}CH_4$ versus $\delta^{13}C{-}CO_2$ indicated methane formation via methyl type reduction, rather than by CO_2 reduction (Fernández et al., submitted).

The presence of both reduced saturated hydrocarbons and oxidized carboxylic acids implied reversible states of redox-dependent metastable equilibrium regulated by hydration and oxidation; i.e. controlled by hydrogen and oxygen fugacities. Thermodynamically, both reduced and oxidized hydrocarbons are in partial equilibrium with bi-/carbonate under oxidation states highly reduced, below those of iron-oxide assemblage and even at the verge stability of water (Wieland and Hummel, 2015). Therefore, oxygen, mineral assemblages and water played an integral role in regulating the redox state and activities of all species involved, by acting as oxidizing agents (terminal electron acceptors, TEAs) and a sink for generated H_2 through redox dependent processes: a) sulfate reduction to H_2S, b) reduction of Fe-oxides (e.g., hematite and goethite) to magnetite and siderite, c) pyrite to siderite, and d) reduction of Fe(III)-bearing phyllosilicates.

Because the stability of aqueous low molecular weight of n-alkanes and other hydrocarbons is highly sensitive to the redox state (Seewald,

2001a; b; Shock, 1988), they were degraded by oxidation depending on the redox buffer in the system. The continuous entrance of oxygen acted as a self-feedback of oxic C-steel corrosion producing iron (III) oxides and hydrocarbons, the last ones being in turn oxidized generating reducing conditions and oxygen consumption. H_2 generated in the process was consumed in further biotic and abiotic reactions (Fernández, 2018). This is consistent with the instability of Fe-oxyhydroxides relative to siderite, as well as the reduction of sulfates from pore water to sulfides. Indeed, apart from Fe-oxyhydroxides, other type of corrosion products, such as siderite (Supplementary Fig. S16) and sulfides (Supplementary Fig. S18), were detected by XRD and SEM analyses (Table 1, Table 2), indicating localized reducing conditions and bentonite pore waters at the liner/Heater #2-bentonite interface with non-negligible concentrations of sulfides and carbonates (> 1 mol/L), precipitating the dissolved Fe^{2+} generated during corrosion and iron alteration. A decrease of the alkalinity of the pore waters was observed as a function of the Heater #2 contact both in aqueous leaching tests (Fig. 10) and squeezed pore waters (Fernández et al., 2018), indicating carbonate precipitation. Furthermore, the hematite (and goethite) generated during oxic corrosion was partially reduced by the organic compounds producing magnetite and dissolved Fe(II) ions, which may have diffused away. This is probably the reason for the red corroded bentonite surrounded by green halos, which were observed in the bentonite samples taken during dismantling operations, as well as the presence of both hematite (and/or goethite) and magnetite iron mineral phases; i.e., Fe(III) and Fe(II) mineral phases.

The indicator of n-alkane oxidation by oxidizing agents (not only oxygen) and/or water is the oxygenated organic species found in the aqueous extracts and squeezed pore waters (Fernández et al., 2018). Carboxylic acids, such as acetate, formate and oxalate were dissolved in the pore water acting as a sink of O_2 and H_2 (Supplementary Table S5). The rate of hydrocarbon oxidation is controlled by oxygen fugacities at temperatures higher than 88 °C and by microbial activity at lower temperatures (Shock, 1988). In absence of reduced saturated hydrocarbons produced by the FT synthesis, the presence of both siderite and iron(II) sulfides should imply highly reducing conditions or the presence of sulfate reducing bacteria (SRB), reducing the sulfates from the pore water to sulfides, taking into account that FEBEX bentonite does not contain sulfides (Fernández et al., 2004). However, the effective abiotic or thermo-chemical reduction of sulfates is only observed at high temperatures (> 200–250 °C), the reaction being too slow at low temperatures unless it is catalysed by sulfate-reducing bacteria (SRB), which have an optimum growth at 80–95 °C (e.g., Libert, et al., 2011). At 90 °C, the extrapolated half-life of the sulfate reduction is ~210,000 years (Truche et al., 2009). Although, some SRB could be cultivated in some bentonite blocks at different sections from the FEBEX *in situ* test, the presence of microorganisms at temperatures higher than 70 °C and close to the Heater#2 contact has not been proved (Bengtsson et al., 2017).

Due to the high contents of chlorides in the pore water at the Heater #2 contact (Fig. 10), also the precipitation of GR-Cl-green rusts and other chloride salts was expected, which were detected by SEM (Table 2, see Fernández et al., 2018). Cl-bearing Fe(III) oxyhydroxide (akaganeite) was detected in other samples analysed (Wersin and Kober, 2017). In turn, the high salinity of the pore water close to the Heater #2 interface favoured corrosion processes.

The extent of line/Heater #2 corrosion was reduced and/or inhibited on time, at least partially, due to possible passivation. Hydrocarbon oxidation rate decreased over time due to the increase of hydrogen and consumption of oxygen (Fernández et al., submitted). Dissolved Fe(II) was consumed on different precipitation reactions (siderite, sulfides, etc.), preventing the diffusion of Fe(II) through outer parts of the bentonite barrier. Indeed, the corrosion processes close to liner/Heater#2 were quite localized affecting the bentonite in the highest altered zone to a maximum thickness of 200 mm, as observed by the blueish-greenish color at the frontal part of Heater #2 (Wersin and Kober, 2017).

5.4. Smectite structural stability

The smectite alteration mechanisms (thermodynamics and kinetics) depend on different factors: temperature, pH, initial smectite composition and ionic strength of the fluid solution and its chemical composition (e.g, Zysset and Schindler, 1996; Herbert et al., 2004). Smectites can be transformed into other minerals as soon as the chemical composition allows to precipitate a more stable phase. However, the equilibrium of clay minerals is a question still open to debate (Blanc et al., 2013).

The presence of two newly formed Mg phases in the FEBEX *in situ* test, brucite and saponite, is important with respect to the understanding of the reactions taking place. In a dissolution-precipitation transformation, quartz precipitates as some montmorillonite layers are dissolved. The chemical balance of this reaction also implies the crystallization of a Mg-rich component that was supposed to precipitate in the interlayer (Howard and Roy, 1985), or as a separate phyllosilicate phase (Meunier, 2005). Brucite was unambiguously proven by different labs by different methods (XRD, FTIR, TG-DTA-DSC), and proves that a solid-state reaction is not only the reason for the Mg accumulation, and dissolution/crystallization reactions are involved in montmorillonite transformation, apart from the advective(-diffusion) process of soluble salts towards the Heater#2 during the saturation of the bentonite barrier.

However, both dissolution/precipitation and solid-state transformations seems to be involved in the FEBEX *in situ* test. The most discussed smectite solid-state alteration mechanism is the development of high charge expandable layers replacing the low-charge layers of the starting montmorillonite, which is linked to an increase in the tetrahedral charge, the altered samples having a mixed montmorillonite (S)-vermiculite (V)/beidellite (B) composition. The development of a highly negative charge on the 2:1 layers leads either to a dehydration of the interlayer cation, or to a loss of protons from the hydrated interlayer cation to form a hydroxide interlayer. Al^{3+} must move into tetrahedral sheets to produce the net positive charge necessary for electrical neutrality, balanced by an increase in interlayer cations (Eberl, 1978; Beaufort et al., 2001). Total layer charge increases because a tetrahedral charge is added to the original octahedral, when Si is replaced by Al (Meunier et al., 2000).

The solid-state transformation was inferred by the TEM-EDX-studies, which allows to distinguish reaction paths from low-charge (LC) montmorillonite particles to high-charge (HC) beidellite or illite, as well as, I/S-ML and diV/S ML in the sense of Środon et al. (1992) and Nguyen-Thanh et al. (2010, 2014). The diV/S MLs are characterised by a K- charge-deficiency with vermiculite layer charge ranging from high charges (HC) of 0.9 eq/h.u.c. to low charges (LC) of 0.65 eq/h.u.c. The trends of the possible reactions involved were determined by using graphical projections in the MR^{3+}-$2R^{3+}$-$3R^{2+}$ system. It is observed in Fig. 8 that most of the samples belong to the stability field of a low-medium layer charge montmorillonite, as the reference FEBEX bentonite, but the samples close to the liner/Heater #2 contact the layer charge increased, as well as the tetrahedral charge and the octahedral magnesium content. Thus, this solid-state transformation produces high-charge/low charge bi-substituted layers similar to vermiculite ones, due to the high content of magnesium at liner/Heater#2 contact. The dehydration of interlayer cations is hindered due to the presence of divalent cations (especially Ca) with a high hydration energy.

Kaufhold et al. (2016) investigated the possibility of a solid-state transformation of dioctahedral smectites to trioctahedral smectites by Mg addition to octahedral vacancies demonstrating that Mg can occupy octahedral sites, but in lower extent than monovalent ions (Li^+), and it can only reach the vacancy when it is really dry (120 °C). Therefore, the implication of Fe(II) in the smectite destabilization and this solid-state transformation should be further analysed.

The oxidation state of Fe in the octahedral sheets affects the layer charge and the reduction of structural Fe(III) to Fe(II) implies an increase of this parameter. Crystal structure must change in order to accommodate the larger size of Fe(II) and the increased negative charge. Some of the Fe atoms migrate from cis- to trans-sites in the reduced state. This migration is necessarily accompanied by a dehydroxylation reaction due to the protonation of OH groups initially coordinated to Fe. Hadi et al. (2013) also observed the dehydroxylation of the structure during Fe(III) to Fe(II) reduction. Such a structural modification would result in the formation of small trioctahedral Fe(II) clusters or domains separated of clusters of vacancies or defect cavities (Manceau et al., 2000; Komadel et al., 2006). This should explain the presence of an additional tv dehydroxylation peak in the TG-DSC signals, apart from the cv dehydroxylation peak from the reference dioctahedral montmorillonite.

The oxidation of native iron to Fe^{2+}, enhanced by temperature, is recognized as the main driving force for smectite dissolution, since the reducing potential of oxidation of iron raises pH to become alkaline and increases dissolution of Si from clay particles. As described by Lantenois et al. (2005) metal Fe is probably the proton acceptor triggering smectite deprotonation during its oxidation process. Both the oxidation of metal Fe and the deprotonation of smectite are strongly favoured by the accessibility of metal Fe to smectite interlayers (Charlet and Tournassat, 2005). In turn, deprotonation increases considerably the layer charge deficit in the smectite octahedral sheets, enhancing their reactivity. Thus, deprotonation may be the driving force for the oxidation of metal ions, and for the initiation of smectite destabilization. However, as discussed above, another process is also involved in the case of the FEBEX *in situ* test. Because the presence of oxygen (and/or other oxidants), the oxidation of hydrocarbons generated by the C-steel corrosion and carbide hydrolysis (see gas evolution during the FEBEX *in situ* test, Fernández, 2018; Fernández et al., submitted) could provoke the Fe(III) reduction of iron oxyhydroxides and smectite and, as consequence, smectite deprotonation, increasing the layer charge which was compensated by the migration of Al^{3+} into tetrahedral sheets, an increase in divalent interlayer cations depleting Na^+ and, finally, the migration of Fe^{2+} and Mg^{2+} to octahedral sites. In addition, as described in literature, dissolved Fe^{2+} cations in pore water probably migrate in its interlayers to compensate for the increased layer charge, favouring the Fe^{2+}-for-Na^+ cation exchange. It is likely that Fe^{2+} cations migrate either into the di-trigonal cavities of smectite tetrahedral sheets or into the smectite octahedral sheets, which is favoured due to the absence of protons inside the di-trigonal cavity and no electrostatic repulsion (Lantenois et al., 2005). This migration is similar to that of Li^+ cations involved in the Hofmann-Klemen test under dry conditions (Hoffmann and Klemen, 1950; Greene-Kelly, 1952). Reduced and adsorbed Fe^{2+} would create structural sites, which would favour adsorption of Mg^{2+} because of its almost equal ionic radius, and the filling of structural vacancies after cationic valence changes. All these mechanisms are not really proved experimentally, so they should be considered in further studies.

The cation substitutions at octahedral sites were analysed by TEM, TG-DSC and FTIR analyses. In Table 5, the Al(IV), Mg + Fe/Al(VI) Fe/Al (VI) and Fe(II) composition ratios are described for the samples analysed. The samples showing a cis-vacant configuration (Table 5), according to Muller et al. (2000), are the FEBEX reference sample and BBIL samples with a high Fe content at octahedral sites (shown by the νMgFe-OH bending band). The high amount of iron should imply an increase in the trans-vacant positions. However, only one dehydroxylation peak is observed corresponding to cis-vacant positions, probably because the Fe(II) content is lower than 6 wt.%, Fe(III) filling cis sites (Tsipursky and Drits, 1984). In other protrusion samples (e.g., BMS-47-2, BMS-53-2, RV-42, BSH), the total magnesium and total Fe(II) content are higher than for the other altered and reddish samples, and show two dehydroxylation peaks and, hence, a cis-trans-vacant configuration. In addition, brucite and saponite were detected in these samples, which was not observed in the BBIL samples, brucite being found when Fe(II) content was above 12 wt.%. Therefore, most of the samples with high amount of Mg^{2+} and Fe(II) at octahedral sites show a cis-trans vacant configuration indicating the formation of interstratified minerals, possibly due to the segregation and clustering of octahedral sheets containing Mg^{2+} and Fe^{2+} cations. The entrance of Mg^{2+} to octahedral sites could be enhanced by Fe(III) reduction and the deprotonation of smectite. Only if the amount of Al(VI) is lower than Mg(VI) content, cis-trans vacant interstratified minerals are formed because in other cases (higher AlAlOH and $AlFe^{3+}OH$ interactions), cis-vacant positions are preserved. The samples with a higher cis-trans interstratifications and the presence of brucite (RV-42 and BSH, Fig. 5) are correlated with a higher Fe^{2+} content, which favours also tv structures and an order/disorder process. This is because the coexistence of cis- and trans-occupied sites within the same octahedral sheet is unfavourable from a crystal chemistry point of view as it violates the principle of local charge balance, so cis and trans sites belong to different layers (Manceau et al., 2000). Al-rich smectites are cis-vacant, whereas for those of high charge and greater tetrahedral charge with Al(IV) in all tetrahedral sheets, and samples with a very high Mg^{2+} and Fe^{2+} contents in octahedral sheets, the trans-vacant configuration is more stable (McCarty and Reynolds, 1995). The tv and cv configurations cannot be together in the same octahedral sheet, but they may occur in different layers, forming an interstratified mineral (Sainz-Díaz et al., 2001; Manceau et al., 2000). Different authors have shown that octahedral cation arrangements are not random at all. Al^{3+} and Fe^{2+} cations tend to segregate from each other (AlAl—OH and $AlFe^{3+}$—OH preferred cis-vacant positions and FeFe—OH trans-vacant positions); whereas Mg^{2+} and Fe^{2+} ($AlFe^{2+}$-, AlMg-, and MgMg-pairs) tend to be dispersed, forming spatial clusters (Marchel and Stanjek, 2012; Cuadros et al., 1999; Sainz-Díaz et al., 2001).

Thus, the presence of saponite (with only Fe^{2+} at octahedral sites) is not correlated with a high corrosion degree and a high Fe content, but only by a high Mg content and cis-trans vacant dehydroxylation peaks, as observed in the BMS samples. For example, in Section 54 (sample BMS-54-xx) the highest MgO increase was observed join with the presence of saponite and brucite, but an iron increase was not detected. This is indicative that corrosion is not the driving force for the trioctrahedralisation process but the structural Fe(III)-bearing smectite reduction induced by the oxidation of saturated reduced hydrocarbons. The reduced Fe(II) migrated from cis to trans sites and further migration of Mg^{2+} to octahedral sites was accompanied with an increase in the negative layer charge and subsequent elimination of structural hydroxyls to maintain constant layer charge, depending of the Fe(II) content (Stucki and Roth, 1977). Due to temperature, high Mg content and Fe(II) reduction, rearrangements in crystal lattice structure due to Mg^{2+} and Fe^{2+} migration towards trans octahedral sites replacing Al^{3+} have produced an order-disorder phenomena, forming cis-trans interstratifications and separated Fe(II) and/or Mg^{2+} trioctahedral domains or clusters separated by diocthaedral domains. Depending on the conditions and the Mg^{2+} and Fe^{2+}content, these domains may be completely segregated forming different phyllosilicate phases: brucite-like sheets, Mg-rich trioctahedral smectite, nontronite or chlorite, evolving to a dissolution/precipitation process. The more Fe(II) content the more segregation, spatial clustering and presence of dispersed brucite-like sheets. Further studies should confirm such processes.

The thermodynamic modelling of Wilson et al. (2006a,b), analysing the Fe-rich phyllosilicate mineral stability at the canister–backfill interface, would explain the Fe(II)-rich clay mineral final products found after Fe(III)-bearing FEBEX smectite reduction. The final products observed in different zones were saponite and chlorite, probably depending on the locally conditions, such as lower temperatures and/or higher depletions in $fO_2(g)$. According with logarithmic activity diagrams, if pore waters are supersaturated with respect to magnetite, Fe (II)-rich saponite would be the most likely montmorillonite alteration product if $fO_2(g)$ values are significantly lower than the

Table 5
Clay mineral structural characteristics detected in the samples at contact with the liner/heater and in the protrusions.

Sample	FEBEX Ref.	BB-47-9	BMS-47-2 mont.	BMS-53-2 mont.	RV-42 Green *mont.*	Liner Red (BBIL-42) *mont.*	Liner Red (BBIL-42) *Nontronite*	Heater Black (BSH) *mont.*	P. Black (BB) *Fe-rich Chlorite*
Al(VI)−Fe(VI) (a)	Al-cis-vacant	**cis-trans vacant**	**cis-trans vacant**	**cis-trans vacant**	**cis-trans vacant**	Al,Fe-cis-vacant	Al,Fe-cis-vacant	**cis-trans vacant**	–
Si/Al(IV)	83	20–36	16	220	21	25	4	15	3
Mg_{tot} + Fe/Al (VI)	0.49	0.31–0.48	0.48	0.56	0.78	**0.56**	**1.83**	0.32	2.52
Mg_{tot}/Al (VI)	0.35	0.19–**0.38**	**0.38**	**0.55**	**0.62**	0.33	0.31	0.32	0.13
Fe/Al(VI)	0.15	0.10	0.10	0.01	0.16	0.22	1.52	0.01	2.40
Dehydroxylation temp	648 °C	598 °C 648 °C	536 °C 658 °C	550 °C 660 °C	528 °C 650 °C	652 °C	652 °C	547 °C 648 °C	588 °C
Saponite	–	?	✓	✓	✓	–	–	✓	–
Brucite	–	–	–	–	✓	–	–	✓	–
νMgFe-OH	–	–	–	–	–	✓	✓	✓	✓
% Fe(II)	0.15 (7%)	n.d.	0.03 (1%)	0.03 (1%)	**0.48 (13%)**	0.11 (2%)	0.13 (2%)	**0.27 (9%)**	22.7 (92.7%)

[a] Smectites may classified into three types based on their octahedral Al^{3+} and Fe^{3+} contents derived from thermal analysis (Muller et al., 2000): a) trans-vacant: those smectites with Al^{3+}(VI) < 1.4 and Fe^{3+}(VI) > 0.3 per $[O_{10}(OH)_2]$; b) cis-vacant: smectites with Al^{3+}(VI) > 1.4 and Fe^{3+}(VI) < 0.3 per $[O_{10}(OH)_2]$, and c) smectites trans-vacant mostly and predominantly ferroan: Al^{3+} (VI) > 1.4 per $[O_{10}(OH)_2]$ and Fe^{3+}(VI) > 0.3 per $[O_{10}(OH)_2]$.

magnetite–hematite equilibrium. But if fO_2(g) exceeds the magnetite–hematite equilibrium, and solutions are saturated with respect to magnetite, berthierine would be more stable than smectite minerals, evolving towards chlorite as a long-term alteration product (Savage et al., 2010, 2014). Berthierine was absent in the FEBEX *in situ* test, but Fe(II)-rich chlorite was found. It is interesting to note that trioctahedral smectites were only identified in the vicinity of the corroding iron in other large experiments, being absent when the heaters were made of copper (Svensson, 2015).

5.5. Modification of physico-chemical properties: CEC and external surface area

The total cation exchange capacity and BET surface area decreased in the samples at close contact with the liner/Heater #2 by around 11–35% and 43–65%, respectively, with respect to the reference value of the FEBEX bentonite. This may be related with a lower content of smectite in the bentonite samples or to a modification of the crystal structure of the smectite particles at this interface. The variation in smectite and total phyllosilicates content in most of the samples seem to maintain in values similar to the reference FEBEX bentonite value. Thus, other explanations need to be given.

A decrease in the CEC may be caused by: a) the collapse of clay particles, particularly of highly charges smectites (Kaufhold and Dohrmann, 2010), b) the collapse of clay particles caused by large ionic strength, which generally reduce the swelling pressure (e.g. Karnland et al., 2006; Herbert et al., 2008), c) extensive drying process due to increased Ca/Mg fixation and/or K fixation at interlayer sites (Kaufhold and Dohrmann, 2010b), d) the formation of Al−Mg-hydroxide complexes in the smectite interlayer (Howard and Roy, 1985), e) the formation of trioctahedral clusters of reduced Fe^{2+} (Hadi et al., 2013), and f) interlamellar collapse due to an dehydroxylation process produced because the Fe(II) migration from cis-sites to trans-sites when structural Fe(III) is reduced to Fe(II) (Stucki and Roth, 1977). As shown by the results all these factors: increase of layer charge, Fe(III)-bearing smectite reduction, high salinity and drying, are involved in the bentonite-liner/Heater#2 interface.

Missana et al. (2018) analysed the size of clay colloids as a function of the exchangeable cation and layer charge location, showing that the presence of above 80% divalent cations at exchange sites favours the formation of large particles, but also that an increase in tetrahedral charge produces an increase in clay colloid size, independently of the main interlayer cation. In the case of the FEBEX retrieved samples at contact with the liner/Heater #2, sodium at exchange sites is almost absent (around 7%), increasing the bivalent cations around 93%. This would imply an increase of the particle size, decreasing the external surface area. In addition, the colloid properties (size and mobility) of the clay minerals are also affected by the electrolyte concentration. The aggregation of clay particles can occur due to the increase of ionic strength because of the diminution of the electrostatic repulsion between the particles which mainly leads to face to face, FF, interactions. Because the increase of the pore water salinity at the heater contact, an increase of the size of clay particles is expected. However, other authors associated the reduction of the surface area by growth of larger and more compact aggregates when possible smectite dissolution and recrystallization of I/S and/or trioctahedral clay minerals (saponite and/or Chl/S mixed layers) are involved (Whitney and Velde, 1993).

On the other hand, it is well-known that redox reactions modify the chemical and physical properties of Fe-containing smectites (Stucki, 2011). The reduction of structural Fe(III) to Fe(II) affects fundamental properties of smectites including layer charge, cation exchange capacity (CEC), cation fixation, specific surface area, swelling behaviour, color and magnetic exchange interactions. In general, reduction induces dehydroxylation or loss of structural OH with increasing Fe^{2+} content (Drits and Manceau, 2000; Roth and Tullock, 1973; Stucki and Roth, 1977), and increases the negative layer charge, the hydration of smectite surface and the cation exchange capacity, while the interlayer cations become less exchangeable (Stucki and Kostka, 2016; Komadel et al., 1995; Stucki and Roth, 1977). The extent of layer charge increase is compensated by (partial) interlayer collapse, which also leads to a decrease of swelling capacity, specific surface area, interlayer spacing, interlayer swelling and hydraulic conductivity of clay minerals (Neaman et al., 2003; Stucki, 1988; Shen et al., 1992; Gates et al., 1998; Kostka et al., 1999). The Fe(II) content increased in the samples at contact with the liner/Heater #2, especially the protrusion samples, i.e., a Fe(III) reduction is observed, which implies a destabilization of the smectite structure and, as consequence, a possible modification of the bentonite properties (Neaman et al., 2003; Stucki, 1988; Shen et al., 1992).

Although the decrease of the external surface area was detected in other samples close to the Heater #2 taken during the dismantling after 18 years of experiment (see Villar et al., 2017) and in samples close to the Heater #1 after 5 years of experiment (see Fernández et al., 2018), the decrease of CEC and external surface area are restricted to the samples at very close contact with the liner/heater the rest of bentonite samples analysed from the FEBEX *in situ* tests preserving its physico-chemical properties.

6. Conclusions

An important issue for performance assessment is to demonstrate the long-term preservation of the bentonite properties. The dismantling of the second part of the FEBEX *in situ* test provided the opportunity to quantify the modifications of the bentonite after iron- and Mg-rich porewater-bentonite interactions at real conditions of a HLW repository system after 18 years of experiment.

The initial compacted bentonite, with a water content of 14% and 1.60 g/cm^3 of dry density after emplacement, evolved towards a fully saturated system after 18 years of experiment, except in the blocks located at the Heater#2 contact, where the saturation degree was around 85–92% (Villar et al., 2016). During the infiltration of the surrounding granitic groundwater, more soluble salts of the bentonite were transported towards the inner part of the bentonite barrier by an advective(-diffusive) transport, modifying the pore water chemistry, the composition of the cations at exchange sites and the mineral equilibria, especially the most soluble accessory minerals. The highest salinity values (Na−Mg−Ca−Cl water-type, 0.41 M ionic strength) were detected at the liner/Heater#2 contact, together with the precipitation of carbonates and increase of Ca/Mg at interlayer sites, exchangeable Na being dramatically depleted. Furthermore, significant Mg accumulation was observed at the very contact to the liner/Heater#2, which is related with the presence of saponite (trioctahedral Mg-smectite), brucite, and Fe-rich chlorite; and a modification in the dehydroxylation temperature of the dioctahedral smectite clay mineral particles.

Metal corrosion occurred mainly at oxic conditions because the FEBEX *in situ* test was not a gas-tight system. In addition, air was entrapped inside the construction gaps (between blocks, sealed after saturation; and between liner and heater). However, localized reduced conditions were achieved due to the presence of Fe(II)-mineral phases. Corrosion was represented by an increase of the Fe-content in bentonite samples taken from the first mm from the liner/Heater #2 contact, increasing the values from 3.1 wt.% to 6–19 wt.%; and the presence of corrosion products, mainly a range of Fe-oxyhydroxides (goethite, hematite and magnetite), siderite and sulfides. Neoformed Mg mineral phases were found in localized zones at the liner/heater contact: brucite, saponite and chlorite.

The driving force for the compositional changes of the bentonite and smectite structural changes seems to be the oxidation and hydrolysis of carbon-containing steel, which affected the redox in the bentonite buffer. At the bentonite-C-steel heater interface, Fe oxidation of carbon-containing steel was dominated by oxic corrosion and hydrolysis, leading to the generation of H_2, CO_2 and hydrocarbons (alkanes, alkenes and carboxylic acids) through a similar Fischer-Tropsch (FT) synthesis reaction. Although FEBEX *in situ* test cannot be considered gas-tight, this FT reaction may be produced at both oxic and anoxic C-steel corrosion conditions. The presence of both reduced saturated and oxidized hydrocarbons implied reversible states of redox-dependent metastable thermodynamic equilibrium under oxidation states highly reduced, below the iron-oxide assemblages. Oxygen (due to no gas-tight conditions) and other oxidizing agents (ferric oxides, sulfates, etc.), regulated the redox state and activities of all species involved in the bentonite barrier, being sulfates reduced to H_2S and pyrite, Fe-oxides (hematite/goethite) to magnetite and siderite, and Fe(III)-bearing smectite to saponite and chlorite, depending probably on the fugacity of oxygen.

Therefore, the mechanism for the structural clay mineral alteration seems to be the Fe(III) structural reduction, rather than the C-steel heater/liner corrosion process itself. Because Fe^{2+} cations are more stable in trans sites than in cis sites at octahedral sheets, rearrangements in crystal lattice seem to have formed cis-trans interstratifications favouring the migration of Mg to octahedral sites. Due to the coexistence of cis- and trans-occupied sites within the same octahedral sheet is unfavourable, separated Mg^{2+} trioctahedral domains were formed, which were completely segregated into Mg-rich trioctahedral smectite and/or brucite depending on the amount of Mg and structural Fe(II). It seems that the more Fe(II) content the more segregation, spatial clustering and presence of dispersed brucite-like sheets, apart from saponite.

The migration of Fe^{2+} and Mg^{2+} to octahedral sites was accompanied with an increase in the negative layer charge and, possibly with the elimination of structural hydroxyls to maintain constant layer. Deprotonation of the smectite was compensated by the migration of Al^{3+} into tetrahedral sheets, and an increase of divalent interlayer cations for Na^+. For this reason, high-charge interstratified clay minerals with a cis-trans vacant configuration were observed in the samples. Thus, both a solid-state transformation, producing high-charge/low charge (bi-substituted) layers similar to vermiculite ones; as well as dissolution-precipitation transformation, with the crystallization of a trioctahedral Mg-smectite (saponite), brucite and chlorite, seem to be inferred, probably depending on $f(O_2)$ and temperature. However, further studies should be performed to confirm such processes. Due to an increase in potassium content was not observed, neither in the solid phase and pore water solutions, a further transformation of the high-charge smectite to illite (illitization) is not expected or it will be insignificant.

These mineral transformations, mainly Fe(III) structural reduction, induced changes in some of the physico-chemical properties of the bentonite, decreasing the total cation exchange capacity and BET surface area. However, these mineralogical and physico-chemical changes were restricted to the bentonite at close contact with liner/Heater#2. The rest of bentonite from the FEBEX *in situ* test maintained its performance as an engineered barrier.

Acknowledgements

This work has been carried out in the framework of two projects: FEBEX-II: Full-scale Engineered Barriers Experiment in crystalline host rock, where the dismantling of Heater #1 was financed by ENRESA and the UE Contract FIKW-CT-2000-00016; and the FEBEX-DP Project, where the FEBEX-DP Consortium (NAGRA, SKB, POSIVA, CIEMAT, KAERI) financed the dismantling of Heater #2. The support of the responsible person of the Consortium, Dr. Florian Kober, is greatly acknowledged. Special thanks to colleagues from AITEMIN for the dismantling activities and the collection of samples. We acknowledge to CITIUS (Sevilla, Spain), UCM (Madrid, Spain) and the Chemical Department from CIEMAT for performing the XRF, XRD, TEM and chemical analyses. Two anonymous reviewers and the handling editor helped to improve the manuscript.

Appendix A. Supplementary data

Supplementary data to this article can be found online at https://doi.org/10.1016/j.apgeochem.2018.09.008.

References

Amman, L., Bergaya, F., Lagaly, G., 2005. Determination of the cation exchange capacity of clays with copper complexes revisited. Clay Miner. 40, 441–453.
Blanc, P., Vieillard, P., Gailhanou, H., Gaboreau, S., 2013. Thermodynamics of clay minerals. In: Bergaya, F., Lagaly, G. (Eds.), Handbook of Clay Science, pp. 173–210 (Chapter 6).
Beaufort, D., Berger, G., Lacharpagne, J.C., Meunier, A., 2001. An experimental alteration of montmorillonite to a di + trioctahedral smectite assemblage at 100 and 200 °C. Clay Miner. 36, 211–225.
Bergaya, F., Brigatti, M.F., Fripiat, J.J., 1985. Contribution of infrared spectroscopy to the study of corrensite. Clay Clay Miner. 33, 458–462.
Bengtsson, A., Blom, A., Taborowski, T., Schippers, A., Edlund, J., Pedersen, K., 2017. FEBEX-DP: Microbiological Report. Nagra Working Report NAB 16-015.
Cataldo, F., 2003. Organic matter formed from hydrolysis of metal carbides of the iron peak of cosmic elemental abundance. Int. J. Astrobiol. 2, 51–63.
Charlet, L., Tournassat, C., 2005. Fe(II)-Na(I)-Ca(II) cation exchange on montmorillonite in chloride medium: evidence for preferential clay adsorption of ions pairs in marine environment chemical modelling and XRD profile modelling study. Aquat. Geochem. 11, 115–137.

Cuadros, J., Sainz-Diaz, C., Ramírez, R., Hernández-Laguna, A., 1999. Analysis of Fe segregation in the octahedral sheet of bentonitic illite-smectite by means of FT-IR, 27Al MAS NMR and reverse Monte Carlo simulations. Am. J. Sci. 299, 289–308.
de la Calle, C., Suquet, H., 1988. Vermiculite. In: In: Bailey, S.W. (Ed.), Hydrous Phyllosilicates. Rev Mineral, vol. 19. Mineral Soc. Am., Washington, D.C, pp. 455–496.
Dohrmann, R., Kaufhold, S., Lundqvist, B., 2013. The role of clays for safe storage of nuclear waste. In: In: Bergaya, F., Lagaly, G. (Eds.), Handbook of Clay Science Vol. 5B. Elsevier, pp. 677–710.
Dong, H., 2012. Clay-microbe interactions and implications for environmental mitigation. Elements 8, 113–118.
Drits, V.A., Manceau, A., 2000. A model for the mechanism of Fe^{3+} to Fe^{2+} reduction in dioctahedral smectites. Clay Clay Miner. 48, 185–195.
Drits, V.A., Besson, G., Muller, F., 1995. An improved model for structural transformations of heat-treated aluminous dioctahedral 2:1 layer silicates. Clay Clay Miner. 43, 718–731.
Duro, L., Domènech, C., Grivé, M., Roman-Ross, G., Bruno, J., Källström, K., 2014. Assessment of the evolution of the redox conditions in a low and intermediate level nuclear waste repository. Appl. Geochem. 49, 192–205.
Eberl, D.D., 1978. Reaction series for dioctahedral smectites. Clay Clay Miner. 26, 327–340.
Emmerich, K., Madsen, F., Kahr, G., 1999. Dehydroxylation behaviour of heat-treated and steam-treated homoionic cis-vacant montmorillonites. Clay Clay Miner. 47, 591–604.
Farmer, V.C., 1974. The Infrared Spectra of Minerals. Mineralogical Society, pp. 539 Monograph 4.
Fernández, A.M., 2018. Gas and Water Sampling in Different Pipes from the FEBEX in Situ Test at the Grimsel Test Site. Nagra Working Report NAB 16-013.
Fernández, A.M., Jockwer, N., Wieczorek, K., submitted for publication. Evolution of the redox conditions in the FEBEX *in situ* test: outcomes from *in situ* gas and pore water sampling. Appl. Geochem..
Fernández, A.M., Sánchez-Ledesma, D.M., Melón, A., Robredo, L.M., Rey, J.J., Labajo, M., Clavero, M.A., Fernández, S., González, A.E., 2018. Thermo-hydro-chemical (THC) behaviour of a Spanish bentonite after dismantling of the FEBEX *in situ* test at the Grimsel Test Site. Nagra Working Report NTB 16-25.
Fernández, A.M., Villar, M.V., 2010. Geochemical behaviour of a bentonite barrier: results up to 8 years of thermo-hydraulic treatment in the laboratory. Appl. Geochem. 25, 809–824.
Fernández, A.M., Baeyens, B., Bradbury, M., Rivas, P., 2004. Analysis of the pore water chemical composition of a Spanish compacted bentonite used in an engineered barrier. Phys. Chem. Earth 29, 105–118.
Fuentes-Cantillana, J.L., García-Siñeriz, J.L., Franco, J.J., Obis, J., Pérez, A., AITEMIN,Jullien, F., Andra,Alberdi, J., Barcala, J.M., Campos, R., Cuevas, J., Fernández, A.M., Gamero, E., García, M., Gómez, P., Hernández, A., Illera, A., Martín, P.L., Melón, A.M., Missana, T., Ortuno, F., Pardillo, J., Rivas, P., Turrero, M.J., Villar, M.V., Mingarro, M., Pelayo, M., CIEMAT,Caballero, E., Cuadros, J., Huertas, F., Huertas, F.J., Jiménez de Cisneros, C., Linares, J., CSIC-Zaidín,Bazargan-Sabet, B., Ghoreychi, M., G.3S,Jockwer, N., Wieczorek, K., GRS,Kickmaier, W., Marschall, P., Nagra,Martínez, M.A., SGS Tecnos, S.A.,Carretero, P., Dai, Z., Delgado, J., Juncosa, R., Molinero, J., Ruiz, A., Samper, J., Vázquez, A., ULC,Alonso, E., Carrera, J., Gens, A., García-Molina, A.J., Guimera, J., Guimaraes, L.do N., Lloret, A., Martínez, L., Olivella, S., Pintado, X., Sánchez, M., UPC-DIT,Elorza, F.J., Borregón, J.L., Canamon, I., Rodriguez Pons-Esparver, R., UPM,Fariña, P., DM Iberia, S.A.,Farias, J., Geocontrol, S.A., 2000. FEBEX Full-scale Engineered Barriers Experiment for a Deep Geological Repository for High Level Radioactive Waste in Crystalline Host Rock Final Report. were the technical editors of this report under the direction of Huertas, F. (Enresa). Enresa, Technical Report 1/2000.
García-Siñeriz, J.L., Abós, H., Martínez, V., De la Rosa, C., Mäder, U., Kober, F., 2016. FEBEX DP: Dismantling of Heater 2 at the FEBEX in situ Test. Description of Operations. pp. 92 Nagra Report NAB 16–11.
Gates, W.P., Jaunet, A.M., Tessier, D., Cole, M.A., Wilkinson, H.T., Stucki, J.W., 1998. Swelling and texture of iron-bearing smectites reduced by bacteria. Clay Clay Miner. 46, 487–497.
Gorski, C.,A., Klüpfel, L.E., Voegelin, A., Sander, M., Hofstetter, T.B., 2013. Redox properties of structural Fe in smectites: 3. Relationships between smectite redox and structural properties. Environ. Sci. Technol. 47, 13477–13485.
Greene-Kelly, R., 1952. A test for montmorillonite. Nature 170, 1130–1131.
Gregg, S.J., Sing, K.S.W., 1982. Adsorption, Surface Area and Porosity. Academic Press, pp. 303.
Hadi, J., Tournassat, C., Ignatiadis, I., Greneche, J.M., Charlet, L., 2013. Modelling CEC variations versus structural iron reduction levels in dioctahedral smectites. Existing approaches, new data and model refinements. J. Colloid Interface Sci. 407, 397–409.
Herbert, H.-J., Kasbohm, J., Sprenger, H., Fernández, A.M., Reichelt, C., 2008. Swelling pressures of MX-80 bentonite in solutions of different ionic strength. Phys. Chem. Earth 33, 327–342.
Herbert, H.J., Kasbohm, J., Henning, K.H., 2004. Long-term behaviour of the Wyoming bentonite MX-80 in high saline solutions. Appl. Clay Sci. 26, 275–291.
Hoffmann, U., Klemen, R., 1950. Verlust der Austauschfähigkeit von Lithiumionen an Bentonit durch Erhitzung. Z. Anorg. Allg. Chem. 262, 95–99.
Howard, J.J., Roy, D.M., 1985. Development of layer charge and kinetics of experimental smectite alteration. Clay Clay Miner. 33, 81–88.
Huertas, F., Fariña, P., Farias, J., García-Siñeriz, J.L., Villar, A.M., Fernández, A.M., Martín, P.L., Elorza, F.J., Gens, A., Sánchez, M., Lloret, A., Samper, J., Martínez, M.A., 2006. FEBEX Project. Full-scale Engineered Barriers Experiment for a Deep Geological Repository for High Level Radioactive Waste in Crystalline Host Rock. Updated Final Report 1994-2004. Technical Publication ENRESA 5-0/2006. pp. 590 (Madrid).
Jackson, M.L., 2005. Soil Chemical Analysis. Advanced Course, revised second ed. Parallel Press. University of Wisconsin-Madison Libraries, Madison, Wisconsin, pp. 930.
Karnland, O., Olsson, S., Dueck, A., Birgersson, M., Nilsson, U., Hernan-Håkansson, T., Pedersen, K., Nilsson, S., Eriksen, T.E., Rosborg, B., 2009. Long-term Test of Buffer Material at the Äspö Hard Rock Laboratory, LOT Project. Final report on the A2 test parcel. TR-09-29. Svensk Kärnbränslehantering AB (SKB), Stockholm, Sweden.
Karnland, O., Olsson, S., Nilsson, U., 2006. Mineralogy and Sealing Properties of Various Bentonites and Smectite Rich Clay Materials. SKB Technical Report TR-06-30. SKB, Stockhlom, Sweden, pp. 112.
Kaufhold, S., Dohrmann, R., Ufer, K., Kober, F., submitted for publication Interactions of bentonite with metal and concrete from the FEBEX experiment. Mineralogical and geochemical investigation of selected sampling sites. Clay Miner..
Kaufhold, S., Dohrmann, R., Götze, N., Svensson, D., 2017. Characterisation of the second parcel of the alternative buffer material (ABM) experiment – I mineralogical reactions. Clay Clay Miner. 65, 27–41.
Kaufhold, S., Dohrmann, R., 2016. Distinguishing between more and less suitable bentonites for storage of high-level radioactive waste. Clay Miner. 51, 289–302.
Kaufhold, S., Dohrmann, R., Ufer, K., 2016. Interaction of magnesium cations with dioctahedral smectites under HLRW repository conditions. Clay Clay Miner. 64, 743–752.
Kaufhold, S., Walter Hassel, A., Sanders, D., Dohrmann, R., 2015. Corrosion of high-level radioactive waste iron-canisters in contact with bentonites. J. Hazard Mater. 285, 464–473.
Kaufhold, S., Dohrmann, R., Sandén, T., Sellin, P., Svensson, D., 2013. Mineralogical investigations of the alternative buffer material test – I. Alteration of bentonites. Clay Miner. 48, 199–213.
Kaufhold, S., Dohrmann, R., 2010. Stability of bentonites in salt solutions: II. Potassium chloride solution. Initial step of illitization? Appl. Clay Sci. 49, 98–107.
Kaufhold, S., Dohrmann, R., 2010b. Effect of extensive drying on the cation exchange capacity of bentonites. Clay Miner. 45, 441–448.
Komadel, P., Madejová, J., Stucki, J.W., 2006. Structural Fe(III) reduction in smectites. Appl. Clay Sci. 34, 88–94.
Komadel, P., Madejová, J., Stucki, J., 1995. Reduction and reoxidation of nontronite: questions of reversibility. Clay Clay Miner. 43, 105–110.
Kostka, J., Wu, J., Nealson, K., Stucki, J., 1999. The impact of structural Fe(III) reduction by bacteria on the surface chemistry of smectite clay minerals. Geochem. Cosmochim. Acta 63/22, 3705–3713.
Kumpulainen, S., Kiviranta, L., Korkeakoski, P., 2016. Long-term effects of an iron heater and Äspö groundwater on smectite clays: chemical and hydromechanical results from the in situ alternative buffer material (ABM) test package 2. Clay Miner. 51, 129–144.
Lantenois, S., Lanson, B., Muller, F., Bauer, A., Jullien, M., Plaçon, A., 2005. Experimental study of smecite interaction with metal Fe at low temperature: 1. Smectite destabilization. Clay Clay Miner. 53, 597–612.
Libert, M., Bildstein, O., Esnault, L., Jullien, M., Sellier, R., 2011. Molecular hydrogen: an abundant energy source for bacterial activity in nuclear waste repositories. Phys. Chem. Earth 36, 1616–1623.
Madejová, J., 2003. FTIR techniques in clay mineral studies. Vib. Spectrosc. 31, 1–10.
Manceau, A., Lanson, B., Drits, V.A., Chateigner, D., Gates, W.P., Wu, J., Huo, D., Stucki, J.W., 2000. Oxidation-reduction mechanism of iron in dioctahedral smectites: I. Crystal chemistry of oxidized reference nontronites. Am. Mineral. 85, 133–152.
Marchel, C., Stanjek, 2012. Cation ordering in cis-and trans-vacant dioctahedral smectites and its implications for growth mechanisms. Clay Miner. 47, 105–115.
McCarty, D.K., Reynolds, R.C., 1995. Rotationally disordered illite-smectite in paleozoic K-bentonites. Clay Clay Miner. 43, 271–284.
Meunier, 2005. Clays. Springer, pp. 472.
Meunier, A., Lanson, B., Beaufort, D., 2000. Vermiculitization of smectite interfaces and illite layer growth as a possible dual model for illite-smectite illitization in diagenetic environments: a synthesis. Clay Miner. 35, 573–586.
Missana, T., Alonso, U., Fernández, A.M., García-Gutiérrez, M., 2018. Colloidal properties of different smectite clays: significance for the bentonite barrier erosion and radionuclide transport in radioactive waste repositories. Appl. Geochem. 97, 157–166.
Moore, D., Reynolds, R., 1989. X-Ray Diffraction and the Identification and Analysis of Clay Minerals. Oxford University Press, N.Y., pp. 332.
Mosser-Ruck, R., Cathelineau, M., Guillaume, G., Charpentier, D., Rousset, D., Barres, O., Michau, N., 2010. Effects of temperature, pH and iron/clay and liquid/clay ratios on experimental conversion of dioctahedral smectite to berthierine, chlorite, vermiculite or saponite. Clay Clay Miner. 58, 280–291.
Muller, F., Drits, V., Plancon, A., Robert, J.L., 2000. Structural transformation of 2:1 dioctahedral layer silicates during dehydroxylation-rehydroxylation reactions. Clay Clay Miner. 48, 572–585.
Neaman, A., Gullaume, D., Pelletier, M., Villieras, F., 2003. The evolution of textural properties of Na/Ca-bentonite following hydrothermal treatment at 80 and 300 °C in the presence of Fe and/or Fe oxides. Clay Miner. 38, 213–223.
Nguyen, L., Herbert, H.J., Hoang-Minh, T., Ferreiro Mählmann, R., 2014. Effects of chemical structure on the stability of smectites in short-term alteration experiments. Clay Clay Miner. 62, 425–446.
Nguyen-Thanh, L., Kasbohm, J., Hoang-Minh, T., 2010. How to calculate mineral formula for 2-member dioctahedral mixed layers from EDX-analysis by Transmission Electron Microscopy: example-Friedland clay. In: 2010 SEA-CSSJ-CMS. Trilateral Meeting on Clays. Sevilla, Spain, 6-11 June. Clay Minerals Society.
Olsson, S., Jensen, V., Johannesson, L.-E., Hansen, E., Karnland, O., Kumpulainen, S., Kiviranta, L., Svensson, D., Hansen, S., Lindén, J., 2013. Prototype Repository. Hydro-mechanical, Chemical and Mineralogical Characterization of the Buffer and Tunnel Backfill Material from the Outer Section of the Prototype Repository. Svensk Kärnbränslehantering AB (SKB), Stockholm, Sweden TR-13–21.

Pelayo, M., Marco, J.F., Fernández, A.M., Vergara, L., Melón, A.M., Pérez del Villar, L., 2018. Infrared and mössbauer spectroscopy of Fe-rich smectites from Morrón de Mateo bentonite deposit (Spain). Clay Miner. 53, 17–28.
Roth, C.B., Tullock, R.J., 1973. Deprotonation of nontronite resulting from chemical reduction of structural Fe(III). In: Serratosa, J.M., Sánchez, A. (Eds.), Proceedings of the International Clay Conference. División de Ciencias, Madrid, Madrid, pp. 107–114.
Russel, J.D., 1987. Infrared methods. In: Wilson, M.J. (Ed.), A Handbook of Determinative Methods in Clay Mineralogy. Blackie, New York, pp. 133–173.
Sainz-Díaz, C.I., Hernández-Laguna, A., Dove, M.T., 2001. Theoretical modelling of cis-vacant and trans-vacant configurations in the octahedral sheet of illites and smectites. Phys. Chem. Miner. 28, 322–331.
Savage, 2014. An Assessment of the Impact of the Long Term Evolution of Engineered Structures on the Safety-relevant Functions of the Bentonite Buffer in a HLW Repository. NAGRA Technical Report 13–02. pp. 62.
Savage, D., Watson, C., Benbow, S., Wilson, J., 2010. Modelling iron-bentonite interactions. Appl. Clay Sci. 47, 91–98.
Sawhney, B.L., 1970. Potassium and cesium ion selectivity in relation to clay mineral microstructure. Clay Clay Miner. 18, 47–52.
Seewald, J.S., 2001a. Model for the origin of carboxylic acids in basinal brines. Geochem. Cosmochim. Acta 65, 3779–3789.
Seewald, J.S., 2001b. Aqueous geochemistry of low molecular weight hydrocarbons at elevated temperatures and pressures: constrains from mineral buffered laboratory experiments. Geochem. Cosmochim. Acta 65, 1641–1664.
Shen, S., Stucki, J.W., Boast, C.W., 1992. Effects of structural iron reduction on the hydraulic conductivity of Na-smectite. Clay Clay Miner. 40, 381–386.
Shock, E.L., 1988. Organic acid metastability in sedimentary basins. Geology 16, 886–890.
Środon, J., Elsass, F., McHardy, W.J., Morgan, D.J., 1992. Chemistry of illite-smectite inferred from TEM measurements of fundamental particles. Clay Miner. 27, 137–158.
Stucki, J.W., 2011. A review of the effects of iron redox cycles on smectite properties. Compt. Rendus Geosci. 343, 199–209.
Stucki, J.W., 1988. Structural iron in smectites. In: Stucki, J.W., Goodman, B.A., Schwertmann, U. (Eds.), Iron in Soils and Clay Minerals. D. Reidel, Dordrecht, pp. 625–675.
Stucki, J.W., Kostka, J.E., 2016. Microbial reduction of iron in smectite. Compt. Rendus Geosci. 338, 468–475.
Stucki, J.W., Roth, C.B., 1977. Oxidation-reduction mechanism for structural Fe in nontronite. Soil Sci. Soc. Am. J. 41, 808–814.
Svensson, D., 2015. The Bentonite Barrier. Swelling Properties, Redox Chemistry and Mineral Evolution. Doctoral dissertation, Faculty of Engineering, Lund University, Sweden.
Svensson, D., Dueck, A., Nilsson, U., Olsson, S., Sandén, T., Lydmark, S., Jägerwal, D., Pedersen, K., Hansen, S., 2011. Alternative Buffer Material. Status of the Ongoing Laboratory Investigation of Reference Materials and Test Package 1. Swedish Nuclear Fuel and Waste Management Company Technical Report SKB TR-11-06.
Tarafder, P.K., Thakur, R., 2012. An optimised 1,10-Phenathroline method for the determination of ferrous and ferric oxides in silicate rocks, soils and minerals. Geostand. Geoanal. Res. 37, 155–168.
Tsipursky, S.I., Drits, V.A., 1984. The distribution of octahedral cations in the 2:1 layers of dioctahedral smectites studied by oblique-texture electron diffraction. Clay Miner. 19, 177–193.
Tournassat, C., Steefel, C.I., Bourg, I.C., Bergaya, F., 2015. Natural and engineered clay barriers. In: Developments in Clay Science, vol. 6. Elsevier, pp. 432.
Truche, L., Berger, G., Destrigneville, C., Guillaume, D., Giffaut, E., Pages, A., 2009. Experimental reduction of aqueous sulphate by hydrogen under hydrothermal conditions: implication for the nuclear waste storage. Geochem. Cosmochim. Acta 73 4824–4835.
Van der Marel, H.W., Beutelspacher, H., 1976. Atlas of Infrared Spectroscopy of Clay Minerals and Their Mixtures. Elsevier, Amsterdam, pp. 396.
Villar, M.V., Iglesias, R.J., Abós, H., Martínez, V., de la Rosa, C., Manchón, M.A., 2016. FEBEX-DP: onsite analysis report. Nagra Working Report NAB 16-012.
Villar, M.V., Fernández, A.M., Romero, E., Dueck, A., Cuevas, J., Plötze, M., Kaufhold, S., Dohrmann, R., Iglesias, R., Sakaki, T., Voltolini, M., Zheng, L., Kawamoto, K., Kober, F., 2017. FEBEX-DP: Post-mortem THM/THC Report. Analysis of Results. Nagra Working Report NAB 16-017.
Wersin, P., Kober, F., 2017. Metal Corrosion and Iron-Bentonite Interaction Studies. Nagra Report NAB 16-16.
Wersin, P., Birgersson, M., Olsson, S., Karnland, O., Snellman, M., 2007. Impact of Corrosion-derived Iron on the Bentonite Buffer Withing the KBS-3H Disposal Concept. The Okiluoto Site as Case Study. Posiva Report 2007-11. Finland.
Wieland, E., Hummel, W., 2015. Formation and stability of ^{14}C-containing organic compounds in alkaline iron-water systems: preliminary assessment based on a literature survey and thermodynamic modelling. Mineral. Mag. 79, 1275–1286.
Wilson, J., Cressey, G., Cressey, B., Cuadros, J., Ragnarsdottir, K.V., Savage, D., Shibata, M., 2006a. The effect of iron on montmorillonite stability (II) Experimental investigation. Geochem. Cosmochim. Acta 70, 323–336.
Wilson, J., Cressey, G., Cressey, B., Cuadros, J., Ragnarsdottir, K.V., Savage, D., Shibata, M., 2006b. The effect of iron on montmorillonite stability. (I) Background and thermodynamic considerations. Geochem. Cosmochim. Acta 70, 306–322.
Whitney, G., Velde, B., 1993. Changes in particle morphology during illitization: an experimental study. Clay Clay Miner. 41, 209–218.
Zysset, M., Schindler, P.W., 1996. The proton promoted dissolution kinetics of K-montmorillonite. Geochem. Cosmochim. Acta 60, 921–931.